remote sensing

MDPI

Article

A Spatially Comprehensive Water Balance Model for Starch Potato from Combining Multispectral Ground Station and Remote Sensing Data in Precision Agriculture

Thomas Piernicke [1,*], Matthias Kunz [1], Sibylle Itzerott [1], Jan Lukas Wenzel [2], Julia Pöhlitz [2] and Christopher Conrad [2]

[1] Section Remote Sensing and Geoinformatics, GFZ Helmholtz Centre for Geosciences, Telegrafenberg, 14473 Potsdam, Germany
[2] Department of Geoecology, Institute of Geosciences and Geography, Martin Luther University Halle-Wittenberg, von-Seckendorff-Platz 4, 06120 Halle (Saale), Germany
* Correspondence: thomas.piernicke@gfz.de

Highlights

What are the main findings?

- Strong correlation between *NDVI* and crop coefficient (*Kc*) derived from Arable Mark 2 ground station data regarding starch potatoes.
- Successful cross-calibration of *NDVI* values from Arable Mark 2 ground stations with remote sensing–based *NDVI* (DJI Phantom 4 multispectral, PlanetScope, and Sentinel-2) of starch potatoes, ensuring consistency between ground-based and satellite/UAV sources.

What is the implication of the main finding?

- Enables the derivation of high-resolution, spatially distributed crop coefficient and water balance maps for starch potatoes from multiple remote sensing platforms.
- Provides a transferable and cost-effective model for precision irrigation in starch potato cultivation and potentially other crops.

Abstract

The measurement of available water for agricultural plants is a crucial parameter for farmers, particularly to plan irrigation. However, an area-wide measurement is often not trivial as there are several inputs and outputs of water into the system. Here, we present a high-resolution, remote sensing-based water balance model for starch potato cultivation, combining multispectral ground station data with UAV and satellite imagery. Over a three-year period (2021–2023), data from Arable Mark 2 ground stations, DJI Phantom 4 MS drones, PlanetScope satellites, and Sentinel-2 satellites were collected in Mecklenburg–Western Pomerania, Germany. The model utilizes *NDVI*-based crop coefficients (R^2 = 0.999) to estimate evapotranspiration and integrates on-farm irrigation and precipitation data for precise water balance calculations. A correlation with reference *NDVI* observations by Arable Mark 2 systems can be shown for UAV (R^2 = 0.94), PlanetScope satellite data (R^2 = 0.94), and Sentinel-2 satellite data (R^2 = 0.93). We demonstrate the model's ability to capture intra-site heterogeneity on a precision farming scale. Our spatially comprehensive model enables farmers to optimize irrigation strategies, reducing water and energy use. Although the results are based on sprinkler irrigation, the model remains adaptable for advanced irrigation methods such as drip and subsurface systems.

check for updates

Academic Editor: Kevin Tansey

Received: 11 July 2025
Revised: 8 September 2025
Accepted: 12 September 2025
Published: 18 September 2025

Citation: Piernicke, T.; Kunz, M.; Itzerott, S.; Wenzel, J.L.; Pöhlitz, J.; Conrad, C. A Spatially Comprehensive Water Balance Model for Starch Potato from Combining Multispectral Ground Station and Remote Sensing Data in Precision Agriculture. *Remote Sens.* **2025**, *17*, 3227. https://doi.org/10.3390/rs17183227

Keywords: sustainable agriculture; irrigation; crop coefficient; Sentinel-2; PlanetScope; drone; UAV; water balance; starch potato; evapotranspiration

1. Introduction

Irrigation is a central topic in modern agriculture, especially due to climate change and the associated increase in variability of temperatures and precipitation. Coupled with the growing global population, farmers face the challenge of optimizing crop yields while conserving resources at the same time [1,2]. In this context, the resource 'water' is of paramount importance. Irrigation strategies need to be designed to adequately meet the water requirements of crops while minimizing water loss.

Particularly for potato and starch potato (*Solanum tuberosum*) cultivation in Germany, significant yield declines and increases in irrigation demand are projected under various Representative Concentration Pathways (RCPs) [3–6]. In other European countries, potato yields have already declined markedly in recent years due to climate change or are expected to do so [2,7–9].

Starch potatoes differ from conventional table potatoes primarily in their higher starch content and are predominantly used in the industry for the production of starch products such as paper, adhesives, and food. Owing to this industrial application, both the quantity and quality of the yield are of considerable economic importance. Optimal water supply is a crucial factor directly influencing both yield and quality. However, starch potato cultivation presents specific irrigation requirements, since water demand varies substantially across different growth stages. During the tuber initiation phase and subsequent tuber growth, water requirements are particularly high [10–12]. Insufficient water supply during this period can result in substantial yield losses, whereas excessive irrigation increases the risk of diseases such as tuber rot. Moreover, the water requirements of starch potatoes are highly dependent on soil and climatic conditions. In regions with low or irregular precipitation, artificial irrigation thus becomes an indispensable agricultural practice.

Various irrigation techniques have been established in agriculture to improve water use efficiency and reduce overall consumption [13]. These include drip irrigation, subsurface irrigation and sprinkler irrigation [14]. Drip irrigation has proven particularly effective, as it delivers water directly to the plant roots, thereby minimizing evaporation losses. However, it requires installation and removal before and after each growing season. Subsurface irrigation is even more efficient but equally demanding in terms of use and maintenance. Sprinkler irrigation, by contrast, is less efficient because considerable amounts of water are lost through evaporation and wind drift, yet it remains versatile and relatively easy to operate. In parallel, new technological developments such as soil moisture sensors and automatic irrigation systems offer additional potential to optimize water use while ensuring stable yields. Publicly available solutions are provided by the German Weather Service (DWD). Among these, AMBAV 2.0 ("Agrameteorologische Berechnung der aktuellen Verdunstung 2.0" or "Agrometeorological Calculation of Actual Evaporation 2.0") estimates actual evapotranspiration using a mixed-source approach that combines the classical Penman–Monteith method with a complex soil hydraulic model [15]. The model also accounts for precise phenological development of the specific crop type and incorporates the coupled feedback of soil drying on plant water uptake dynamics [16]. However, with a spatial resolution of 1×1 km, its applicability for precision agriculture remains limited. In addition, international providers such as Arable Labs (www.arable.com, accessed on 11 July 2025) Inc. and Pessl Instruments (https://metos.global/de/, accessed on 11 July 2025)

offer commercial solutions. A common limitation of these systems, however, is that they do not adequately capture intra-site-specific heterogeneities.

To achieve optimal efficiency, it is essential that irrigation is implemented at a precision farming level through intra-site-specific applications, since precision agriculture (PA) represents a key component of sustainable agricultural practices in the 21st century [17–19]. Although multiple definitions of PA exist, the underlying concept remains consistent [20]: to understand variations in resource conditions at the intra-field scale and to respond to them appropriately in both temporal and spatial dimensions [21]. Over the past decades, numerous methods have been developed and discussed to estimate crop irrigation needs within the PA framework [22–26]. This is particularly important to prevent plant stress caused by excessively wet or dry conditions and to ensure consistently high yields across entire fields, while conserving water as the most critical resource [17]. In this study, PA is defined as agricultural management with a spatial resolution of up to 5 m—based on the native 3.7 m resolution of PlanetScope data with an added buffer for pixel smoothing and interpolation and a daily temporal resolution.

In recent decades, applications of remote sensing (RS) techniques in agriculture, and particularly for estimating evapotranspiration as the key component of water loss from the plant–soil system, have been extensively reviewed [17,27–30]. Substantial research has specifically focused on irrigation planning using RS-based approaches [17,25,31–34]. Some methods integrate soil moisture conditions through remote sensing. However, these approaches attempt to derive soil moisture directly from satellite observations, which are typically limited by low spatial and temporal resolution and therefore do not meet intra-site-specific requirements. This results in considerable uncertainties regarding both spatial and temporal precision [35–40]. Ground-based methods, such as cosmic-ray neutron sensing or soil sensor-based irrigation management and crop water stress indices, also show reduced accuracy, particularly under closed canopy conditions, as the information density from the soil decreases as canopy cover increases [41–43]. An alternative approach is the estimation of evapotranspiration, and thus, the water balance, based on crop coefficient values derived from high-resolution remote sensing data. This method is applicable at the intra-site-specific scale and does not rely on direct soil moisture measurements [44]. The main challenge, however, lies in obtaining reliable crop coefficient values that correlate with the Normalized Difference Vegetation Index (*NDVI*) at a precision farming scale for near-real-time calculations. In this study, we present a solution based on Arable Mark 2 ground stations in combination with UAV and satellite data.

Over a period of three years (2021–2023), we monitored two sites in Mecklenburg–Western Pomerania, Germany, where our model crop, the starch potato '*Waxy cv. Henriette*,' was cultivated. This was accomplished using multispectral drone imagery, PlanetScope and Sentinel-2 satellite data, together with Arable Mark 2 ground station data, where *NDVI* measurements from the Remote Sensing Sources (RSS) were cross-calibrated against Arable Mark 2 *NDVI* to derive the crop coefficient and, consequently, crop evapotranspiration on the Remote Sensing Sources [45]. While PlanetScope data alone would be sufficient to generate a complete temporal series, occasional gaps are unlikely to be filled by the limited number of Sentinel-2 overpasses but could be addressed by UAV acquisitions. The rationale for including all three sources is to ensure broader applicability: PlanetScope data, although high-frequency and high-resolution, can be cost-prohibitive, limiting practical access to a subset of users. Sentinel-2, by contrast, is freely available and provides a European alternative that can serve as a baseline for water balance estimation. Given that cloud cover can most certainly affect both satellite sources in the DEMMIN area and even Germany-wide, UAVs were included as a third option. UAVs can not only fill temporal or spatial data gaps but also operate independently of satellite imagery, providing high-

resolution information suitable for users without access to satellite data, or for applications requiring very fine spatial resolution, such as implementing precision irrigation systems like drip irrigation.

Additionally, precipitation data were obtained from the RADOLAN product of the German Weather Service [46], and irrigation depths were recorded during irrigation events to determine water input at high spatial resolution.

The aim of this study was to develop a new method to improve the precision of ground station-based water balance estimations by integrating high temporal and spatial resolution UAV, PlanetScope, and Sentinel-2 satellite data, with resolutions of one day and up to three meters, respectively, covering areas of up to 30 ha. This approach enables the optimization not only of sprinkler irrigation but also of drip and subsurface irrigation systems, and provides a practical tool, such as field maps, for farmers to determine when irrigation is required and to adjust irrigation volumes according to specific intra-field needs.

2. Materials and Methods

2.1. Study Site Characterization and Experimental Design

Our field study was conducted at the regional test site DEMMIN (Durable Environmental Multidisciplinary Monitoring Information Network), which extends from 54.04°N to 53.83°N and from 12.97°E to 13.35°E, located in the federal state of Mecklenburg–Western Pomerania around the city of Demmin, approximately 220 km north of Berlin (Figure 1). The DEMMIN site covers 900 km^2, is part of the TERENO-NE observatory, and is intensively used for agriculture. It has served as a scientific observation area for over 20 years investigating climate data and soil moisture observation [47,48].

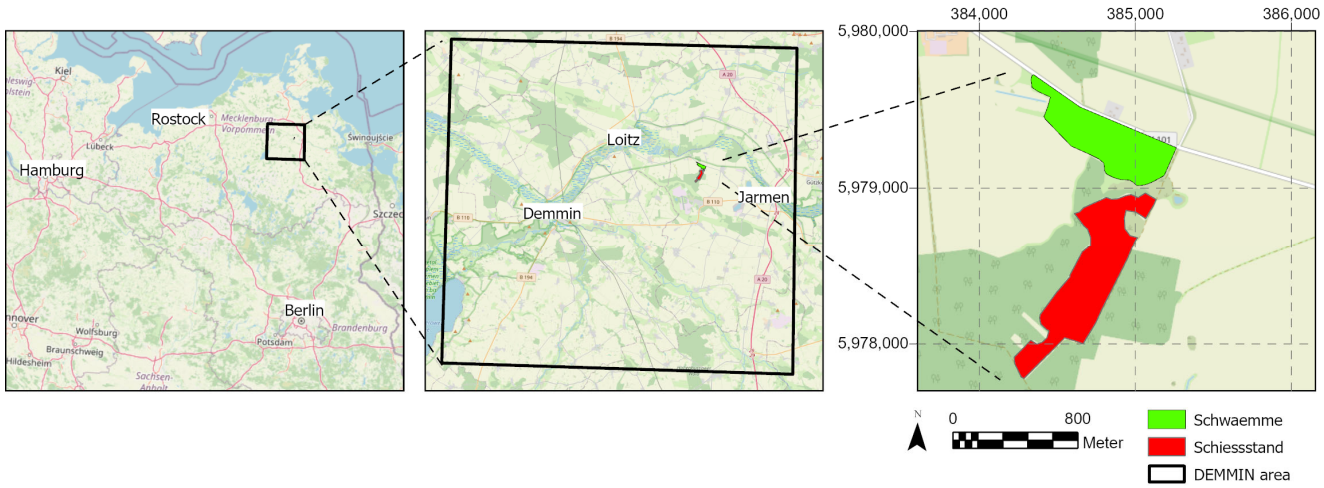

Figure 1. Overview map of the two field sites within the DEMMIN research area in northwestern Germany. Coordinates are given in WGS 84/UTM zone 33N (EPSG:32633).

During the vegetation periods from 2021 to 2023 (May to October each year), our partner farm Bentziner Ackerbau GmbH regularly cultivated the medium-sized high-amylopectin potato (HAPP) "Waxy cv. Henriette" at two sites, "Schwämme" and "Schießstand," both located in the DEMMIN area (Figure 1). Crop management practices followed the standard procedures of the local farmer (Table 1), and the experiment was fully integrated into the farmer's workflow to avoid disruption of regular operations or invasive interventions. The study sites cover 23.7 ha (Schwämme) (Figure 2) and 30.7 ha (Schießstand) (Figure 3). Ridge spacing was 0.75 m, with a plant spacing of 0.38 m. The general soil physicochemical properties revealed site-specific differences and gradients, with sand fraction and soil organic carbon (SOC) varying from west to east at Schwämme and from

north to southwest at Schießstand. Further details on crop management can be found in Wenzel et al. (2022) [49].

Table 1. ANOVA (AOV) comparing UAV-based NDVI models with increasing degrees, i.e., from linear model to 4th degree polynomial model. Best-choice model was found with the 3rd degree model, since R^2 of training and validation are maximized and AIC, BIC, and RMSE as well as RMSE (10 fold cross-validation) are minimized. Significance levels: $p < 0.01$ (**), $p < 0.001$ (***); n.s. = not significant; NA = not applicable.

Dataset	Model Properties	1st Degree	2nd Degree	3rd Degree	4th Degree
training	R^2	0.9388	0.9435	0.9545	0.9548
	AOV Res.Df	104	103	102	101
	AOV RSSq	0.2351	0.2169	0.1747	0.1736
	AOV Df	NA	1	1	1
	AOV SSq	NA	0.0182	0.0422	0.0011
	AOV F	NA	10.5958	24.5574	0.6412
	AOV *p* value	NA	**	***	n.s.
	AIC	−340.955	−347.501	−368.4402	−367.111
	BIC	−332.9647	−336.8472	−355.123	−351.1304
validation	R^2	0.9192	0.9261	0.9293	0.9263
	RMSE	0.0573	0.0544	0.0527	0.0538
	RMSE (10 f-cross)	0.0485	0.0473	0.0429	0.0436

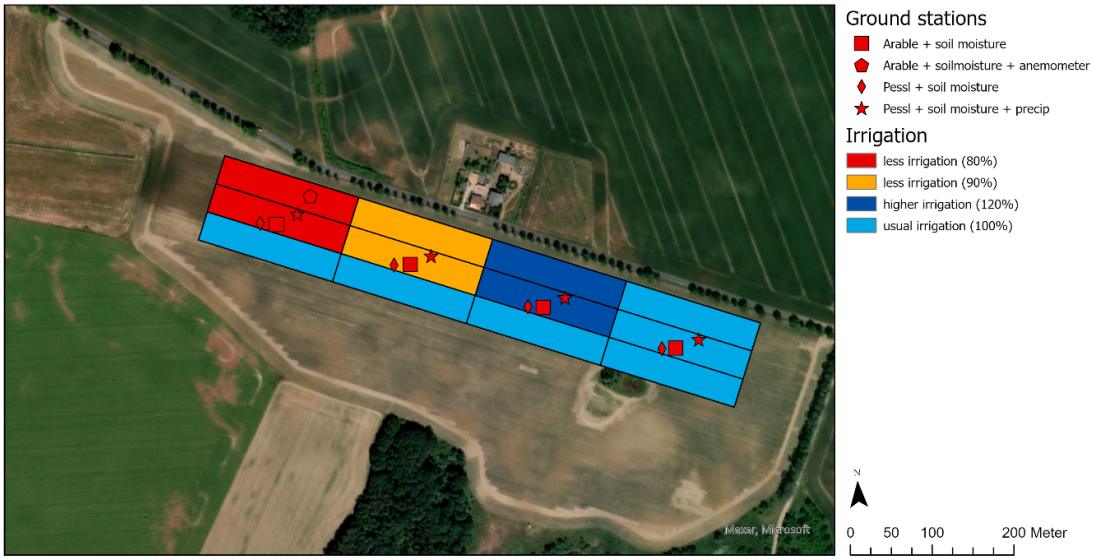

Figure 2. Study site in 2021 showing sprinkler transects with varying and uniform irrigation levels as well as the ground station setup.

In 2021, the experiment was conducted at the "Schwämme" site (center: 53.9495°N, 13.2446°E) and comprised four plots, each measuring 172 m × 72 m (1.24 ha), aligned along a single irrigation lane (Figure 2). Irrigation amounts were varied across the four plots, with 100% serving as the farmer's reference (18–25 mm per irrigation event), based on values derived from the ZEPHYR model [50]. In addition to the reference and control plots (both irrigated at 100%), plots with 80%, 90%, and 120% irrigation levels were established to create two reduced- and one increased-irrigation treatments. Each plot was equipped with one Arable Mark 2 ground station (Arable Labs, Inc., Princeton, NJ, USA) connected to one 60 cm Sentek soil moisture probe (Sentek Sensor Technologies, Stepney, Australia) to record *NDVI*, reference evapotranspiration (ET_{ref}) and crop evapotranspiration (Kc), soil moisture, and meteorological data. Furthermore, two Pessl µMetos® Base-NBIOT weather stations, each connected to a 60 cm Sentek soil moisture probe and one additionally equipped with a

tipping bucket, were installed per plot to record soil moisture and increase the sample size. To account for potential differences in soil type as an explanatory variable, a dense grid of soil core samples was collected across the entire site and in the vicinity of the ground stations prior to the experiment [49].

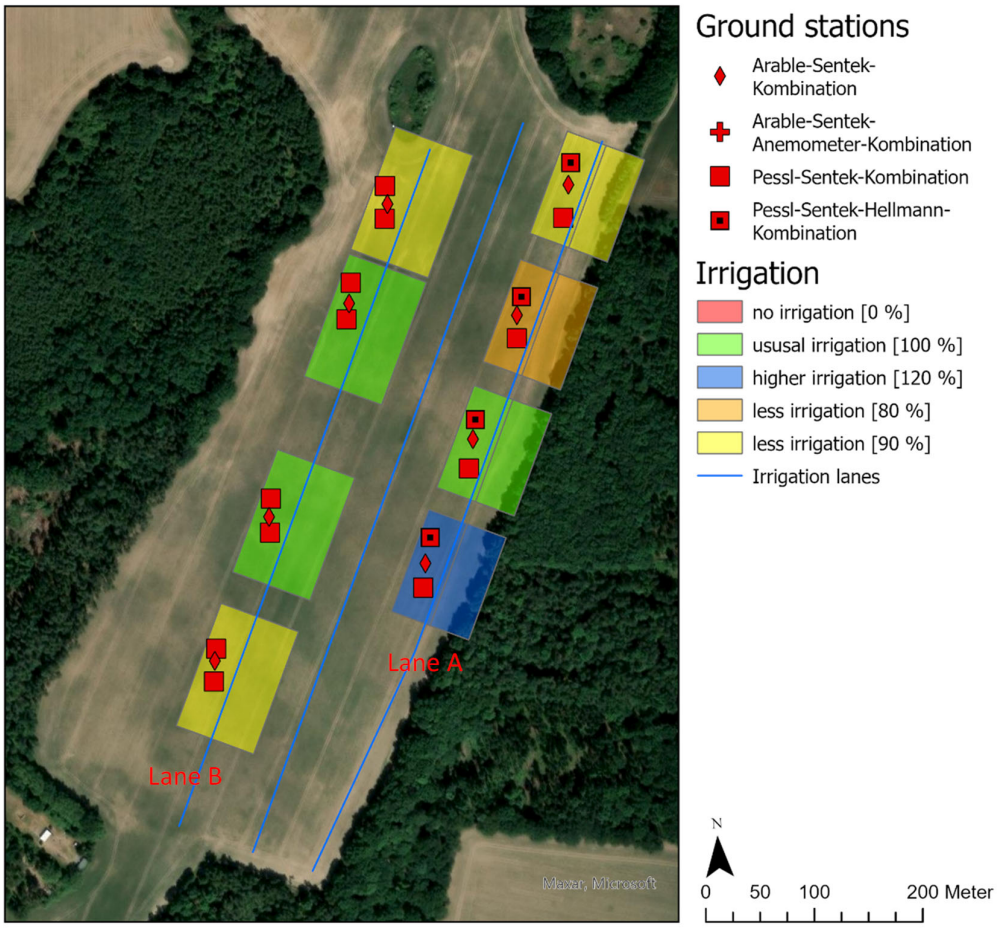

Figure 3. Study site in 2022 showing sprinkler transects (lanes A and B) with varying irrigation levels and the ground station setting.

The experimental setup was repeated in 2022 at the "Schießstand" site (center: 53.941°N, 13.2436°E) following a design similar to that of 2021 to consider other meteorological and field conditions but with an additional irrigation lane to account for different soil types (Figure 3). While the soil along irrigation lane A (eastern lane) was comparable to that of the 2021 site, irrigation lane B (western lane) included both sandy–loamy soil and sandy soil. Four plots were established along lane B using the same configuration as lane A but with a modified treatment. The two northernmost plots were located on sandy–loamy soil, while the two southernmost plots were located on sandy soil [49]. In both soil types, plots were irrigated at 100% and 80%.

In 2023, the experiment was again conducted at the "Schwämme" site but with a modified design complemented by a Closed Path Eddy Covariance System CPEC310 (Campbell Scientific, Loughborough, UK), which was only available in that year. The EC-Systems location was chosen to maximize the observation area according to the field size and form. It was installed at a height of 2.2 m, corresponding to a radius of 220 m and a footprint of 15.21 ha, covering 7.3 ha of the study site and thus including all four irrigation lanes. In total, five Arable Mark 2 ground stations and 16 Pessl ground stations, each connected to a 60 cm Sentek soil moisture probe, were randomly distributed across the site to collect the same set of data as in previous years (Figure 4). Unlike the previous

experiments, no irrigation treatments were varied. Instead, all irrigation was applied at the farmer's reference level of 100%.

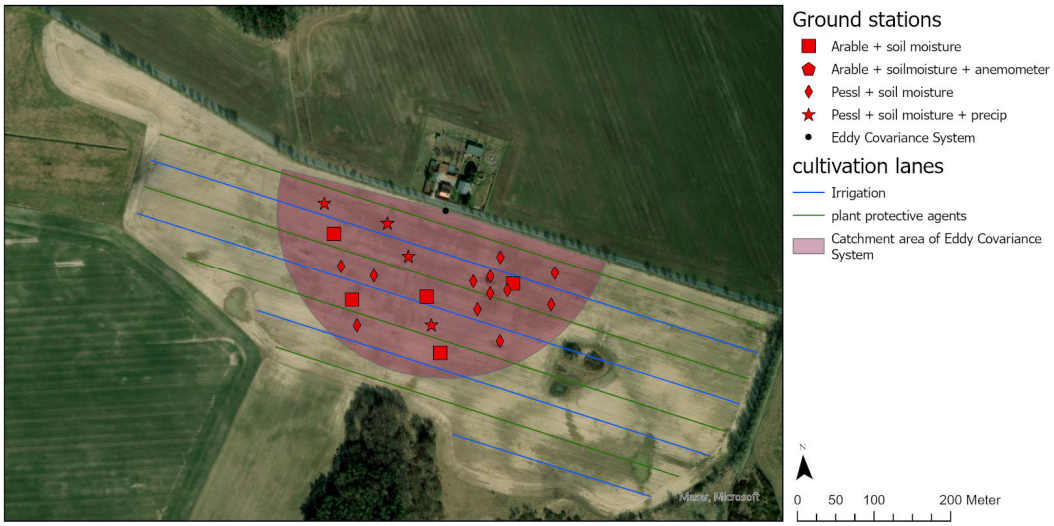

Figure 4. Study site in 2023 with ground station setup and footprint covered by Eddy Covariance System.

2.2. Irrigation Data

Irrigation was applied using a Fasterholt FM 4900H (Fasterholt Maskinfabrik A/S, Brande, Denmark) gun sprinkler [51], which allows irrigation amounts to be adjusted through prior programming. Irrigation volumes were logged with a *Raindancer GPS tracking module* by IT-Direkt Business Technologies GmbH (www.raindancer.com, accessed 11 July 2025). From the user portal, a CSV file containing the most recent 10,000 data points—with a temporal resolution of 7 min (equivalent to the last 12 days)—can be downloaded for each sprinkler and irrigation event, including coordinates, timestamps, and water pressure values. Conversion tables provided in the sprinkler manual [51] were used to derive irrigation heights for a 25.4 mm nozzle under varying water pressure. Missing water pressure values were calculated by linear interpolation. After downloading the irrigation logs, GPS errors were corrected using a floating mean and linear interpolation. The data were then processed into shapefiles containing polygonal circles representing the actual irrigation amounts.

2.3. Precipitation Data

We obtained precipitation data from the German Weather Service product RADOLAN, which is based on weather radar calibrated against climate station data [46,52,53], as well as X-band weather radar data from a Furuno WR-2120 located in Neubrandenburg, approximately 44 km south of the test sites [54]. Additional sources included precipitation measurements from Arable Mark 2 stations, tipping buckets connected to four of the eight Pessl stations, and the nearby climate station "Bentzin". However, the X-band radar proved unsuitable, as its beams were obstructed by trees, leading to interference and incorrect measurements at the test sites. The Arable Mark 2 stations are equipped with an acoustic disdrometer for precipitation measurement, but since they also register irrigation, it was not possible to reliably distinguish between rainfall and irrigation events. For this reason, the DWD RADOLAN product was chosen as the primary source of precipitation data in this study.

2.4. Optical Remote Sensing Data

Since our aim is to derive crop coefficients over larger areas from *NDVI* data, it is first necessary to account for the differences between the optical systems used for point-based

NDVI detection (Arable Mark 2 ground stations) and area-wide *NDVI* detection (UAV and satellite observations).

2.4.1. Arable Mark 2 Optical Measurements

Arable Mark 2 ground stations record 7-band spectral data [55,56], capturing both vegetation-reflected and incoming solar radiation once per hour during daylight. *NDVI* values are derived using band 4 (red) and band 6 (NIR). First, daily data is filtered to measurements that were taken one hour before and one hour after solar noon each day. *NDVI* is then calculated by dividing the upwelling by the corresponding downwelling reflectance values.

2.4.2. UAV Data and Post-Processing

To collect multispectral information at the two sites, we used a DJI Phantom 4 Multispectral UAV (SZ DJI Technology Co., Ltd., Shenzhen, China) (firmware V00.00.0130) equipped with a 5-band multispectral sensor system (2 MP) and an RGB sensor (5 MP). In 2021, only one irrigation lane was observed; in 2022, coverage was extended to three lanes; and in 2023, all four lanes were included. This expansion was implemented because irrigation variability proved greater than expected and could be more effectively captured with a larger observed area. Flights were conducted approximately once per week (Figure 1) during the vegetation periods, depending on weather conditions, using autopilot missions programmed with DJI Ground Station Pro. Flight parameters included an altitude of 100 m, nadir camera orientation, flight paths perpendicular to crop rows, and an overlap of 75% in the forward and 69% in the side direction. This configuration was found to be the most time-efficient for both flight execution and data processing, without compromising data quality. Orthomosaics from each flight were generated in Pix4Dmapper (Pix4D S.A., Prilly, Switzerland; versions 4.6.0 and later 4.8.0) using the standard AG Multispectral configuration [57]. GeoTIFFs were exported from the orthomosaics using all tiles and a transparent background. *NDVI* was calculated using only the red and NIR multispectral bands. The final orthomosaics were manually co-registered in ArcGIS Pro 3.0 to minimize spatial error, with an RMSE <0.2 m and a maximum deviation of 30 cm. Subsequently, the imagery was resampled to the site boundaries to ensure pixel overlays across flights and aggregated to a 5 m resolution to harmonize spatial resolution. Although gun sprinklers are relatively imprecise in irrigation, maintaining high spatial resolution ensures compatibility with more precise irrigation techniques that may be adopted in the future.

2.4.3. PlanetScope Data

We used the PlanetScope dataset for 2021 to 2023 covering the entire DEMMIN area from the Federal Agency for Cartography and Geodesy, "Servicestelle Fernerkundung". Here, we chose the "analytic"dataset aligned to Sentinel-2. The PlanetScope TOA data were converted to surface reflectance values (BOA) using the 6SV2.1 radiative transfer code in combination with MODIS near-real-time atmospheric data, allowing for the correction of atmospheric effects such as aerosol scattering, water vapor absorption, and Rayleigh scattering, and thereby providing reflectance values representative of the actual land surface [58]. The native spatial resolution of 3 m was scaled down to 5 m, so it matches with the UAV data resolution.

2.4.4. Sentinel-2 Data

Sentinel-2 L2A datasets were downloaded via openEO (https://openeo.dataspace.copernicus.eu, accesses on 15 December 2024) after selecting the scenes with less than 10% cloud cover from the Copernicus catalog. The native spatial resolution of 10 m was

resampled to 5 m to enable integration with UAV and PlanetScope data. A summary of data acquisitions from 2021 to 2023 is provided in Figure 5.

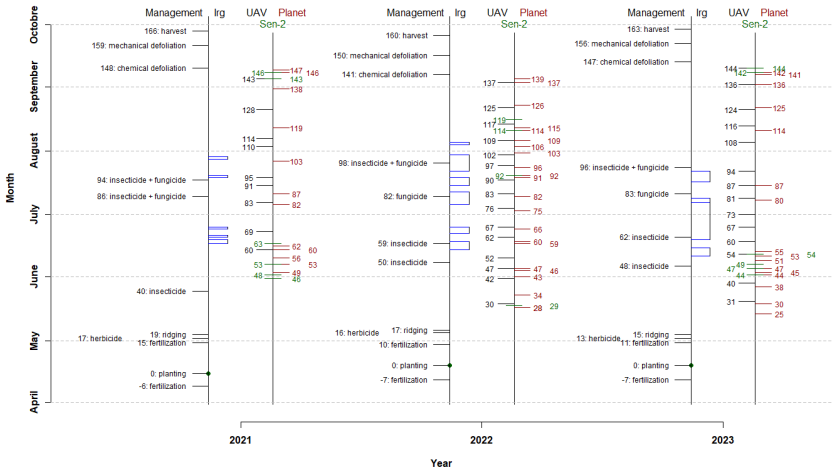

Figure 5. Dates of multispectral flyovers of UAV (black), PlanetScope (red), Sentinel-2 (green), and crop management procedures (left of each timeline, black) according to days after planting (DAP).

2.5. Technical Workflow of Integration of NDVI and Crop Coefficient

Since this study aims to achieve high spatial and temporal resolution of evapotranspiration and water balance, the crop coefficient of every pixel must be known. As Arable Mark 2 stations provide crop coefficients only from pre-trained models for their specific footprint, it is necessary to link the station-derived crop coefficients and *NDVI* with the ability of Remote Sensing Sources (RSS) to observe larger areas (Figure 6). (1) Because the correlation is not publicly available, it must be determined. (2) A cross-calibration of Arable Mark 2 *NDVI* with the *NDVI* from each individual RSS at coincident times is performed to adjust the RSS-based *NDVI* to the Arable Mark 2 reference. (3) The resulting models from steps (1) and (2) are then integrated to calculate crop coefficients Kc_{RSS} for each RSS pixel based on *NDVI*. By multiplying the Kc_{RSS} with reference evapotranspiration, a spatially distributed water balance can be derived (4).

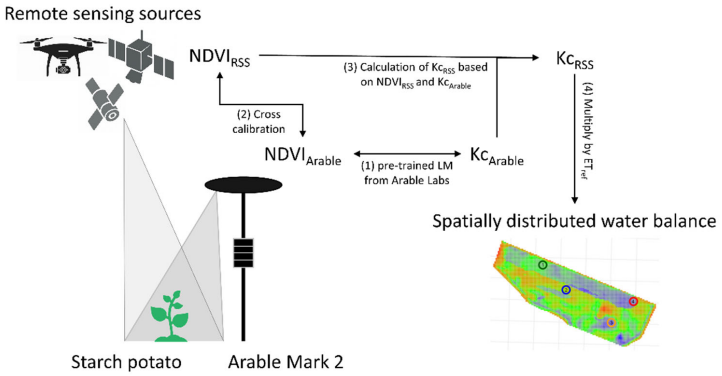

Figure 6. The workflow comprises (1) the correlation of NDVI and crop coefficient based on Arable Labs' pre-trained models for starch potato, (2) an intermediate step involving cross-calibration between NDVI measured by the Arable Mark 2 and each remote sensing source (RSS), and (3) the calculation of crop coefficients from NDVI obtained by each remote sensing source, which can be used to calculate water balance from RSS imagery.

2.5.1. Correlation of Crop Coefficient and *NDVI* from Arable Mark 2 Stations over Three Years

To link *NDVI* with evapotranspiration, we used the crop coefficient derived in this study, since it forms the basis for calculating the water balance. In addition to *NDVI*

calculated from optical data, Arable Mark 2 ground stations estimate the corresponding crop coefficient based on a training dataset experimentally developed by Arable, as well as reference evapotranspiration, both of which are required to derive crop evapotranspiration. This dataset was collected over three cultivation periods, and a correlation between *NDVI* and crop coefficient was established. For our analyses, we used *NDVI* values calculated directly from the individual spectral bands, as the *NDVI* values provided by the Arable stations are pre-flagged and post-processed by Arable through an undisclosed method.

2.5.2. Adjustment of UAV-Based *NDVI* Measurements to Arable Mark 2-Based *NDVI* Measurements

To extend the spot-wise *NDVI* measurements from Arable Mark 2 stations to the entire study sites, we used a DJI Phantom 4 Multispectral UAV. To ensure that the *NDVI*–crop coefficient relationship could also be applied to UAV data, a cross-calibration between ground station-based *NDVI* and UAV-based *NDVI* was performed. First, samples were extracted from UAV *NDVI* orthomosaics using buffers corresponding to the footprint of each Arable Mark 2 ground station. Second, the mean pixel values of each sample were correlated with the *NDVI* values recorded by the respective ground stations. Due to occasional downtimes of Arable Mark 2 stations caused by software errors and the exclusion of measurements taken after the last irrigation event, the sample size was limited to n = 163 over three years. Only measurements collected before the final annual irrigation event were included, as the onset of senescence alters the *NDVI*–crop coefficient relationship. Third, to validate the model, the dataset was randomly divided into a training set (65% of values, n = 106) and a validation set (35% of values, n = 57). Fourth, the training dataset was used to fit polynomial regression models of increasing degree until ANOVA indicated no significant improvement with higher orders. Also, R^2, AIC, and BIC of the models were calculated. Afterwards, R^2 and RMSE were calculated by testing the model on the validation dataset, and RMSE from a 10-fold cross validation was calculated. To minimize overfitting, the final model was selected based on the principle of the minimum adequate model. Fifth, the adjusted UAV-based *NDVI* values were then substituted into the linear model equation to calculate crop coefficients for every pixel of the UAV-based orthomosaics.

2.5.3. Adjustment of PlanetScope-Based *NDVI* Measurements to Arable Mark 2-Based *NDVI* Measurements

Here, the overall sample size of n = 300 was also subdivided, with the training dataset consisting of n = 195 and the validation dataset consisting of n = 105. The subsequent processing steps to establish a correlation between PlanetScope-based *NDVI* and crop coefficient followed the same procedure as described for the UAV correction.

2.5.4. Adjustment of Sentinel-2-Based NDVI Measurements to Arable Mark 2-Based *NDVI* Measurements

Here, the overall sample size of n = 48 was also subdivided, with the training dataset consisting of n = 31 and the validation dataset consisting of n = 17. The subsequent processing steps to establish a correlation between Sentinel2-based *NDVI* data and crop coefficient followed the same procedure as described for the UAV correction.

2.6. Model Setup and Integration of Input Terms

Water balance in this study refers to the climatic water balance equation (Equation (1)), which incorporates negative crop evapotranspiration and positive precipitation and irrigation for each pixel (x,y), and day after planting (DAP) i, while neglecting surface runoff.

$$WB_{i,xy} = \begin{cases} -ETc_{i.xy} + mean(precipitation_i) + irrigation_{i,xy}, & precipitation\ from\ Arable\ Mark\ 2 \\ -ETc_{i.xy} + precipitation_{i,xy} + irrigation_{i,xy}, & precipitation\ from\ Weather\ Radar \end{cases} \quad (1)$$

The daily values are accumulated up to a given day n, when the agronomist needs to initiate the next irrigation event:

$$WB_{n,xy} = \sum_{i=1}^{n} WB_{i,xy} \quad (2)$$

2.6.1. Crop Evapotranspiration

According to FAO 56 [59], daily reference evapotranspiration together with the crop coefficient is used to calculate crop evapotranspiration (*ETc*) for each pixel (*x*,*y*) and day after planting (*i*):

$$ETc_{i,xy} = ETref_i \times Kc_{i,xy} \quad (3)$$

ET_{ref} is predicted by Arable ML model and is based on the FAO Penman–Monteith method [56]. Alternatively, ET_{ref} provided by the German Weather Service can be used, which is modeled on a 1 km grid [60] and also follows the FAO Penman–Monteith approach but relies on physical measurements. The crop coefficient (*Kc*) results from our modeled correlation between UAV-derived *NDVI*, Arable Mark 2 *NDVI*, and the Arable Mark 2 crop coefficient. Since it is based on UAV *NDVI* data, *Kc* represents an individual value for each pixel (*x*,*y*) and is available for each day (*i*) either directly through measurements or by interpolation.

2.6.2. Precipitation

Precipitation and irrigation are required as input terms. With several Arable Mark 2 stations installed at our sites, we calculated daily precipitation as the mean of their measurements and applied this value uniformly to all pixels. Alternatively, weather radar data were used, enabling a spatially explicit application by providing precipitation values for each pixel (*x*,*y*) and each day (*i*).

2.6.3. Irrigation

Each irrigation event was logged with geographic coordinates, date and timestamp, as well as parameters, that allowed calculation of irrigation amounts for every log entry at 7-min intervals (Sections 2.2 and 3.4). Given that the sprinkler irrigates within a radius of approximately 36 m, an intersection query was performed to identify each map pixel (*x*,*y*) within the overlapping sprinkler radii. The irrigation amount for each pixel was then calculated as the mean of the overlapping radii. In the next step, the datasets were aggregated and corrected to match a daily temporal resolution (*i*).

3. Results

3.1. Correlation Between GS-Based Crop Coefficient and NDVI

The Arable Mark 2-based crop coefficient was modeled from *NDVI* from all of the three vegetation periods (Figure 7). Here, a significant coefficient of determination can be achieved (R^2 = 0.999, $F_{(1,1328)}$ = 1,264,000, $p < 0.001$, n = 1330, RSE = 0.02, y = 1.49x − 0.22):

$$Kc_{NDVI\_GS} = 1.49 \times NDVI_{GS} - 0.22 \quad (4)$$

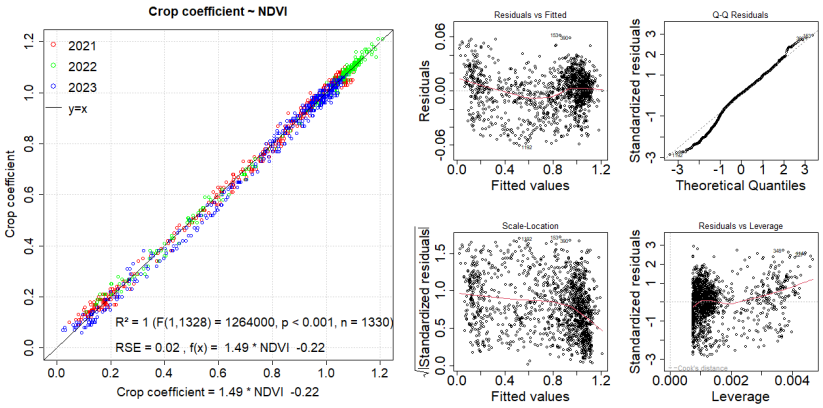

(**a**) (**b**)

Figure 7. (**a**) Correlation of *Kc* and NDVI measured by Arable Mark 2 ground stations across three vegetation periods using five (2021 and 2023) and eight (2022) rsp. ground stations reveals a linear regression and (**b**) residual analysis of *Kc* and NDVI linear regression. "Residuals vs. fitted" shows no distinctive pattern. "QQ-Residuals" shows some very few outliers at the ends (1192, 153, 390), but no value is off the line, so a normal distribution of residuals can be assumed. "Scale location" shows randomly distributed residuals with no distinctive pattern. Even the former outliers are not off the rest of the values, so homoscedasticity can be assumed. "Residuals vs. leverage": although there are some outliers named (114, 227, 348), values do not enter "cooks distance", so there is no influential case in linear regression.

By measuring daily *Kc* and *NDVI* values using five (2021, 2023) and eight (2022) rsp. Arable Mark 2 stations installed in the field over three growing seasons on two different plots, a total of n = 1330 data points were collected, which reveal a linear trend (Figure 7). Despite these temporal and spatial heterogeneities, a residual analysis shows no distinctive pattern or influential outliers, and residual analysis shows no outliers or statistical signals.

3.2. Correlation Between Arable Mark2-Based NDVI and DJI Phantom 4 MS-Based NDVI

To determine the optimal correlation between *NDVI* from Arable Mark 2 ground stations and *NDVI* from the DJI Phantom 4 Multispectral, higher-degree polynomial models were fitted until no further significant improvement was achieved, while minimizing AIC and BIC (Table 1). Model performance was evaluated using the validation dataset, aiming for the highest R^2 and the lowest RMSE, including RMSE from 10-fold cross-validation. The best-fit model was a third-degree polynomial (Figure 8), with all higher-order terms highly significant and the intercept term also significant (Table 2).

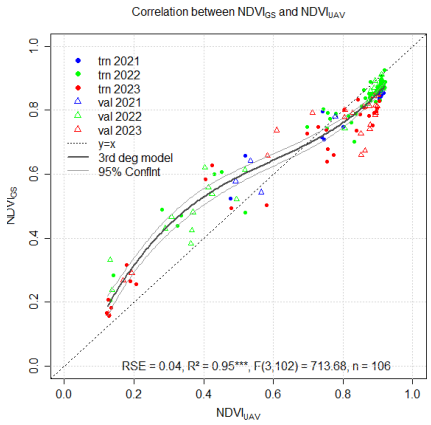

Figure 8. Correlation between NDVI measured by UAV and Arable Mark 2 ground stations (thick solid line = model fit, solid points = training dataset, triangles = validation dataset). The results indicate a third-degree polynomial correlation with RSE = 0.04 and R^2 = 0.95 *** for the training dataset.

Table 2. Estimates, CI, and *p*-values of single degrees of polynomial model of correlation between NDVI values measured by UAV and Arable Mark 2 ground stations.

Predictors	Estimates	CI	*p*
(Intercept)	−0.10	−0.19–−0.01	0.029
NDVI UAV [1st degree]	2.75	2.06–3.44	<0.001
NDVI UAV [2nd degree]	−3.79	−5.20–−2.38	<0.001
NDVI UAV [3rd degree]	2.13	1.28–2.98	<0.001
Observations		106	
R^2/R^2 adjusted		0.955/0.953	

The final model showed a strong correlation between both attributes (R^2 = 0.95 ($F_{(3,102)}$ = 713.7, $p < 0.001$, n = 106, RSE = 0.04):

$$NDVI_{GS} = 2.13 \times NDVI_{UAV}^3 - 3.79 \times NDVI_{UAV}^2 + 2.75 \times NDVI_{UAV} - 0.1 \quad (5)$$

The equations can be joined by employing $NDVI_{GS}$ in Equation (6) to directly calculate the crop coefficient:

$$Kc_{NDVI\_UAV} = 1.49 \times \left(2.13 \times NDVI_{UAV}^3 - 3.79 * NDVI_{UAV}^2 + 2.75 \times NDVI_{UAV} - 0.1\right) - 0.22 \quad (6)$$

3.3. Correlation Between Arable Mark2-Based NDVI and PlanetScope-Based NDVI

The comparison between *NDVI* derived from Arable Mark 2 and PlanetScope was performed in the same manner as for UAV-based *NDVI*. The best-fit model was a fourth-degree polynomial (Table 3) (Figure 9), with all terms highly significant (Table 4). Although a sixth-degree polynomial provided a slightly better fit in terms of R^2, AIC, and BIC, it exhibited clear overfitting at the boundaries of the function domain D = (0.22, 0.92).

Table 3. ANOVA (AOV) was performed to compare PlanetScope-based NDVI models of increasing complexity, ranging from a linear model to a sixth-degree polynomial. The best-choice model was identified as the fourth-degree polynomial, although the sixth-degree model yielded the highest R^2 for both training and validation datasets and minimized AIC, BIC, and RMSE, including RMSE from 10-fold cross-validation. However, due to clear overfitting, the fourth-degree model was selected as the most appropriate. Significance levels: $p < 0.001$ (***); n.s. = not significant; NA = not applicable.

	Model Properties	1st Deg	2nd Deg	3rd Deg	4th Deg	5th Deg	6th Deg
training	R^2	0.9444	0.9477	0.9482	0.9502	0.951	0.954
	AOV Res.Df	193	192	191	190	189	188
	AOV RSSq	0.557	0.5238	0.5195	0.4991	0.4912	0.4605
	ANOVA Df	NA	1	1	1	1	1
	AOV SSq	NA	0.0332	0.0043	0.0203	0.008	0.0307
	AOV F	NA	13.4572	1.7511	8.2354	3.2306	12.4483
	AOV *p* value	NA	***	n.s.	***	.	***
	AIC	−582.9699	−592.9519	−592.5666	−598.3451	−599.4833	−610.0709
	BIC	−573.1509	−579.8599	−576.2016	−578.7071	−576.5723	−583.8869
validation	R^2	0.9312	0.9369	0.9388	0.9392	0.945	0.9489
	RMSE	0.0595	0.0569	0.0561	0.0557	0.053	0.0512
	RMSE (10 f-cross)	0.054	0.0529	0.0526	0.0525	0.0529	0.0509

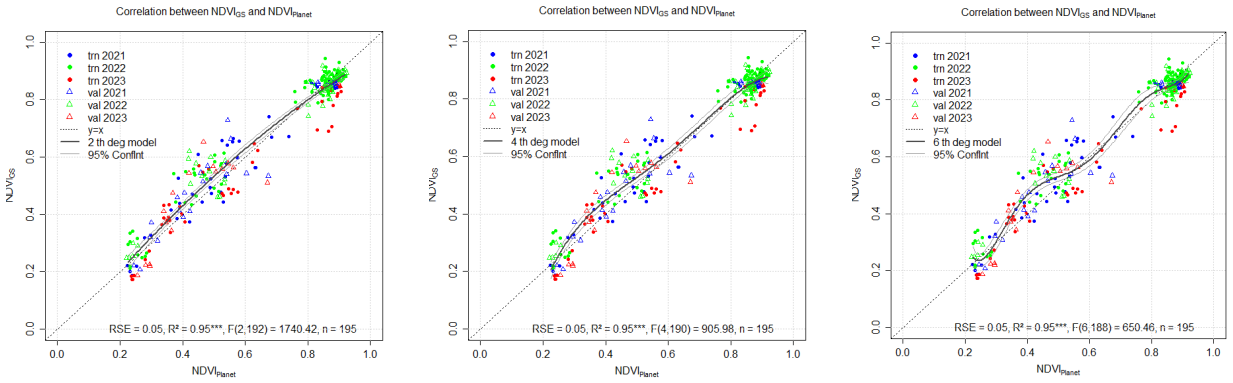

(**a**) (**b**) (**c**)

Figure 9. Correlation between NDVI measured by PlanetScope and by Arable Mark 2 ground stations (thick solid line = model graph, solid points = training dataset, triangles = validation dataset). (**a**) Values show a 2nd degree polynomial correlation for training dataset RSE = 0.05, R^2 = 0.95 ***, AIC = −592.95, BIC = −579.86. (**b**) Values show a 4th degree polynomial correlation for training dataset RSE = 0.05, R^2 = 0.95 ***, AIC = −598.35, BIC = −578.71. (**c**) Values show a 6th degree polynomial correlation for training dataset RSE = 0.05, R^2 = 0.95 ***, AIC = −610.07, BIC = −583.89. Although the 6th degree polynomial model shows the best fit, its graph shows an overfitting at the end of the domain D = (0.22, 0.92), so the 4th degree polynomial model is meant to be the best-choice model.

Table 4. Estimates, CI, and *p*-values of single degrees of polynomial model of correlation between NDVI values measured by PlanetScope and Arable Mark 2 ground stations.

Predictors	Estimates	CI	p
(Intercept)	−0.82	−1.32–−0.32	0.001
NDVI Planet [1st degree]	7.77	3.56–11.98	<0.001
NDVI Planet [2nd degree]	−18.75	−31.02–−6.48	0.003
NDVI Planet [3rd degree]	21.72	6.83–36.61	0.004
NDVI Planet [4th degree]	−9.07	−15.50–−2.64	0.006
Observations		195	
R^2/R^2 adjusted		0.950/0.949	

The final model correlates both attributes with an R^2 = 0.95 ($F_{(4,190)}$ = 905.98, $p < 0.001$, n = 195, RSE = 0.05):

$$NDVI_{GS} = -9.07 \times NDVI_{Plan}^4 + 21.72 \times NDVI_{Plan}^3 - 18.75 \times NDVI_{Plan}^2 + 7.77 \times NDVI_{Plan} - 0.82 \quad (7)$$

The equations can be joined by employing $NDVI_{GS}$ in equation xx to directly calculate the crop coefficient:

$$Kc_{NDVI\_Plan} = 1.49 \times (-9.07 \times NDVI_{Plan}^4 + 21.72 \times NDVI_{Plan}^3 - 18.75 \times NDVI_{Plan}^2 + 7.77 \times NDVI_{Plan} - 0.82) - 0.22 \quad (8)$$

3.4. Correlation Between GS-Based NDVI and Sentinel-2-Based NDVI

The model correlating Sentinel-2-based *NDVI* with Arable Mark 2-based *NDVI* resulted in a second-degree polynomial relationship as best fit model (Table 5) (Figure 10), with all higher-order terms highly significant and the intercept below the first significance level but showing a tendency (Table 6).

Table 5. ANOVA (AOV) was conducted to compare Sentinel-2-based NDVI models of increasing degree, ranging from a linear model to a fourth-degree polynomial. The best-fit model was identified as the third-degree polynomial, as it maximized R^2 for both training and validation datasets while minimizing AIC, BIC, and RMSE, including RMSE from 10-fold cross-validation. Significance levels: NA = not applicable.

Dataset	Model Properties	1st Degree	2nd Degree	3rd Degree
training	R^2	0.9185	0.966	0.9677
	AOV Res.Df	29	28	27
	AOV RSSq	0.1232	0.0513	0.0488
	AOV Df	NA	1	1
	AOV SSq	NA	0.0718	0.0026
	AOV F	NA	36.5762	1.3116
	AOV *p* value	NA	0	0.2644
	AIC	−77.3971	−102.5249	−102.1205
	BIC	−73.0952	−96.789	−94.9506
validation	R^2	0.9491	0.9261	0.9067
	RMSE	0.0442	0.0526	0.0615
	RMSE (10 f-cross)	0.0679	0.0456	0.0457

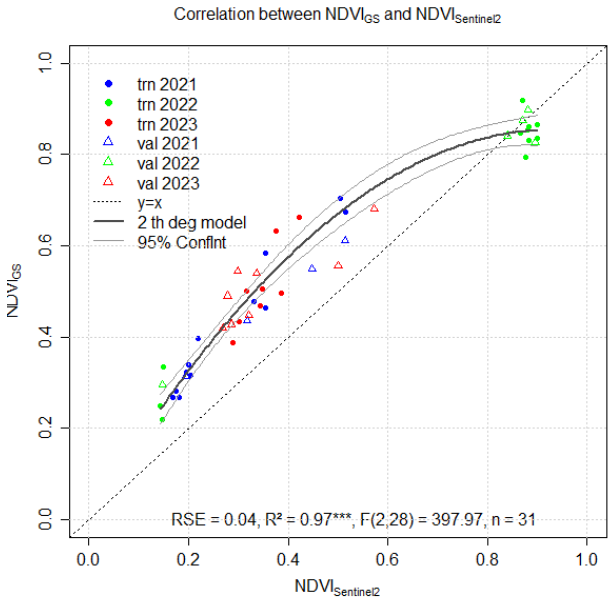

Figure 10. Correlation between NDVI measured by Sentinel-2 and Arable Mark 2 ground stations (thick solid line = model graph, solid points = training dataset, triangles = validation dataset). Results indicate a second-degree polynomial correlation with RSE = 0.04 and R^2 = 0.97 *** for the training dataset.

Table 6. Estimates, CI, and *p*-values of single degrees of polynomial model of correlation between NDVI values measured by Sentinel-2 and Arable Mark 2 ground stations.

Predictors	Estimates	CI	*p*
(Intercept)	−0.00	−0.08–0.07	0.959
NDVI Sen2 [1st degree]	1.84	1.48–2.20	<0.001
NDVI Sen2 [2nd degree]	−0.99	−1.31–−0.66	<0.001
Observations		31	
R^2/R^2 adjusted		0.966/0.964	

The final model correlates both attributes with an $R^2 = 0.97$ ($F_{(2,28)} = 397.97$, $p < 0.001$, n = 31, RSE = 0.04):

$$NDVI_{GS} = -0.99 \times NDVI_{S2}^2 + 1.84 \times NDVI_{S2} - 0.002 \quad (9)$$

The equations can be joined by employing $NDVI_{GS}$ in Equation (10) to directly calculate the crop coefficient:

$$Kc_{NDVI\_S2} = 1.49 \times \left(-0.99 \times NDVI_{S2}^2 + 1.84 \times NDVI_{S2} - 0.0022\right) - 0.22 \quad (10)$$

3.5. Reference Evapotranspiration

Since ET_{ref} values from the Arable Mark 2 stations show only minor noise (RMSE < 0.2 per day) and no significant spatial patterns between stations after flagging (Figure 11), they can be considered uniform across the test sites. Therefore, a daily mean value was used.

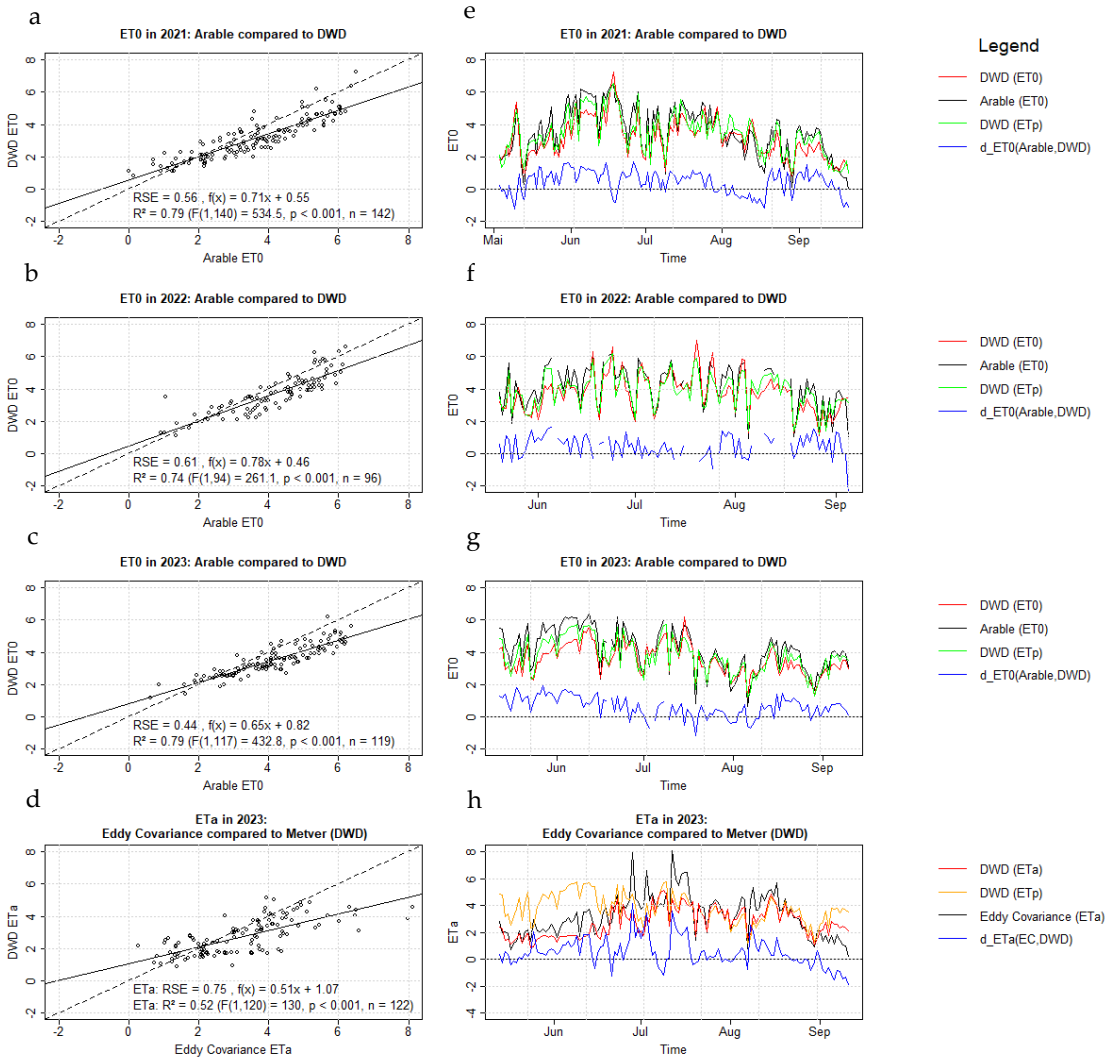

Figure 11. Correlations and temporal trends of reference and actual evapotranspiration from the German Weather Service (FAO56), Arable Mark 2, the on-site Eddy Covariance system, and METVER (DWD) for the vegetation periods of 2021, 2022, and 2023. Across all three years, ET_{ref} correlations show a weaker slope for DWD estimates compared to Arable Mark 2 (**a**–**c**). Temporal trends (**e**–**g**) indicate that DWD values occasionally exceeded those of Arable Mark 2 during extreme events, while the stations generally reported higher values for the remainder of the period. For ET_a in 2023 (**d**,**h**), local EC measurements were consistently higher than METVER (DWD). Both effects are likely attributable to the coarse spatial resolution of the DWD models compared to on-site measurements.

Compared with *ETref* from the German Weather Service (DWD), the Arable-derived values were consistently slightly higher across all years. The coefficient of determination in 2021 was $R^2 = 0.79$ ($F_{(1,140)} = 534.5$, $p < 0.001$, n = 142, RSE = 0.56) rsp., while in 2022, it was $R^2 = 0.74$ ($F_{(1,94)} = 261.1$, $p < 0.001$, n = 96, RSE = 0.61), and in 2023, it was $R^2 = 0.79$ ($F_{(1,117)} = 432$, $p < 0.001$, RSE = 0.44). In general, DWD modeled lower ET_{ref} values compared to Arable, except for certain extreme events when DWD values were higher, which was likely due to the coarser spatial resolution of DWD data (1 km).

Additionally, ET_p and ET_a from DWD were modeled using METVER [61–64] and compared with ET_a derived from the on-site Eddy Covariance System, which applies a model coupling air temperature [°C] and latent heat flux [$W \cdot m^{-2}$]. The METVER-based *ETa* also accounted for the four irrigation events in 2023 (12 June: 21 m^2, 19 June: 25 mm, 3 July: 29 mm, 17 June: 21 mm). *ETa* values from the EC system and METVER showed a fairly consistent trend from May until early June, after which *ETa* measured by the EC system exhibited four distinct peaks that were absent in METVER. Between June and mid-July, EC-based *ETa* was considerably higher, whereas from mid-July to late August, both approaches yielded comparable values. Consequently, the coefficient of determination was relatively low ($R^2 = 0.52$ ($F_{(1,120)} = 130$, $p < 0.001$, n = 122, RSE = 0.75).

3.6. Precipitation Data Acquisition from Multiple Sources

Precipitation was measured using the German Weather Service RADOLAN product, the Furuno WR-2120 X-band weather radar, Arable Mark 2 ground stations, four of the eight Pessl stations equipped with tipping buckets, and the nearby climate station "Bentzin" (1.5 km northeast of Schwämme and 2.2 km northeast of Schießstand). The different measurement methods revealed substantial discrepancies for the comparison years 2022 and 2023 (May 20 to September 10 each year) (Table 7). While results from RADOLAN and the average of the Arable Mark 2 stations were relatively consistent (2022: 216.1 mm for RADOLAN vs. 229 ± 50.1 mm for Arable; 2023: 195.2 mm for RADOLAN vs. 205.8 ± 26.7 mm for Arable), the Furuno radar reported significantly lower values (136.8 mm in 2022 and 100.2 mm in 2023). The Bentzin climate station also recorded markedly low values (81.6 mm in 2022 and 106.6 mm in 2023), likely due to technical issues. The Pessl stations, which rely on a tipping bucket mechanism, exhibited high variability, likely influenced by irrigation events, similarly to the Arable Mark 2 stations. Noticeable patterns emerged: station '0390B89E' consistently recorded the highest precipitation in both years, followed by '0390B885', '0390B88E', and '0390BDD'. The latter two stations reported extremely low totals (<50 mm and as little as 25 mm). Because local ground-based measurements were likely affected by irrigation or technical errors, and as the X-band radar and Bentzin station also failed to provide reliable data, only the DWD RADOLAN product was considered for further analysis. Nonetheless, the model is compatible with other precipitation data sources, particularly X-band radar.

Table 7. Precipitation measured for test sites by different methods in 2022 und 2023 (each year from 20th May till 10th September).

Year	2022	2023
Furuno	136.8 mm	100.2 mm
RADOLAN	216.1 mm	195.2 mm
Climate station Bentzin	81.6 mm	106.6 mm
Pessl 0390B88E	144.1 mm	45.3 mm
Pessl 0390B885	189.2 mm	151.1 mm
Pessl 0390B89E	338.6 mm	293.2 mm
Pessl 0390BDDD	145.6 mm	25 mm
Arable Mark 2 mean	229 ± 50.1 mm	205.8 ± 26.7 mm

3.7. Gun Sprinkler Irrigation

From the raw gun sprinkler data, irrigation maps were generated. While the nozzle size remained constant at 25.4 mm, water pressure and sprinkler speed varied. Water pressure depended on the number of sprinklers operating on the same pump, whereas sprinkler speed was influenced by both water pressure and field morphology (e.g., ascending or descending slopes) as well as soil conditions such as compaction and moisture. An example irrigation event (Figure 12) conducted between 14th and 18th June 2022 shows a mean irrigation amount of 21.4 ± 3.13 mm (n = 579), with values ranging from 18 mm to 57 mm. The highest amounts occurred due to a sprinkler malfunction in the northern section of the westernmost irrigation lane, where the sprinkler slowed and eventually stopped while continuing to irrigate. Correspondingly, sprinkler speed decreased to 12 m/h before reaching a complete stop, compared with a mean speed of 30.4 ± 2.47 m/h (n = 579), within a range of 11.8–36.3 m/h. Water pressure ranged between 4.0 and 4.4 bar, with a mean of 4.23 ± 0.1 bar (n = 579).

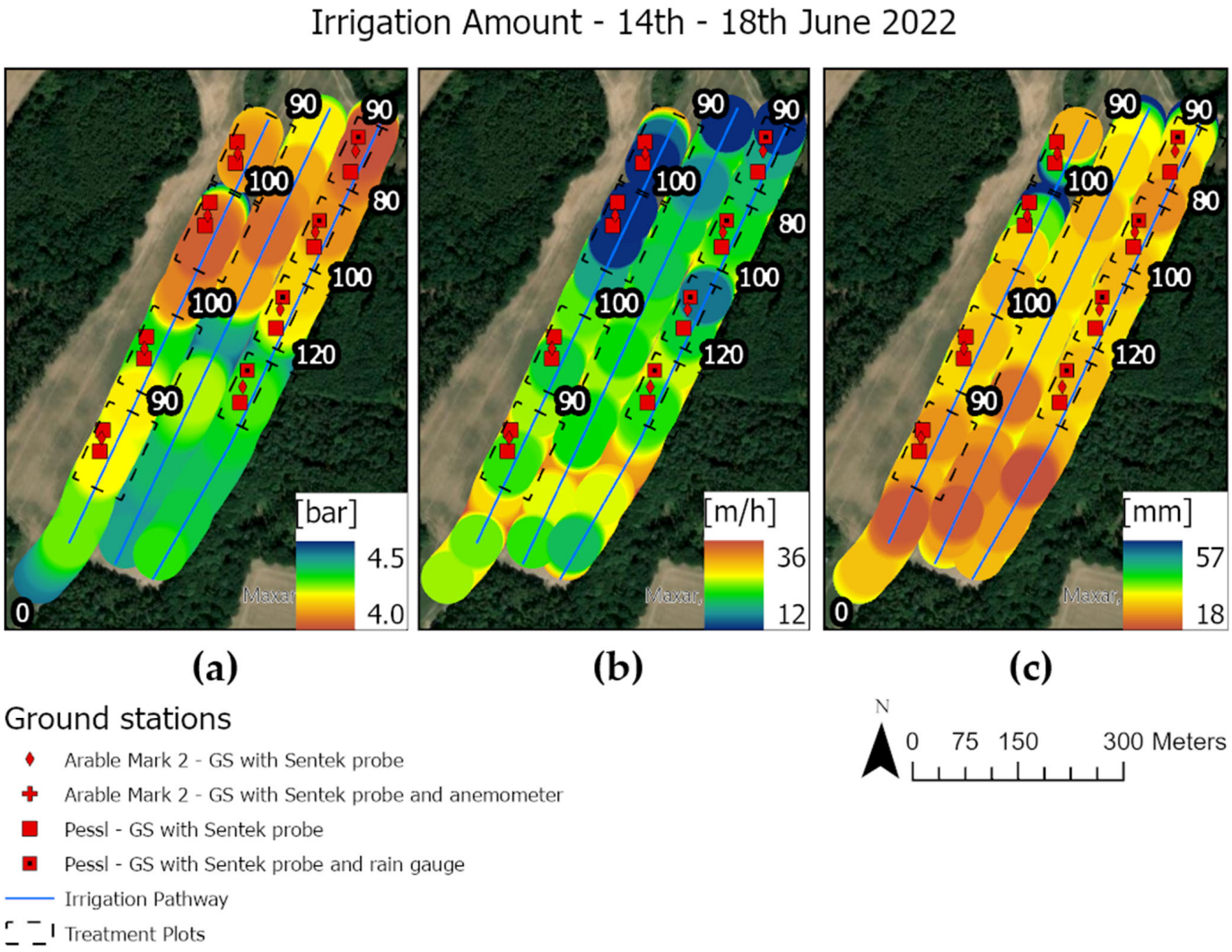

Figure 12. Water Pressure (**a**), sprinkler movement speed (**b**) and irrigation amount (**c**) of the first irrigation event in 2022 (14–18 June 2022). Since sprinkler drive technology directly links water pressure (**a**) and movement speed (**b**), lower pressure results in reduced speed, keeping the applied irrigation amount nearly constant. Variations in irrigation amount (**c**) are mainly attributable to sprinkler malfunction (northwestern section) or to field morphology and soil conditions, respectively.

3.8. Crop Evapotranspiration and Water Balance

Multiplying the pixelwise crop coefficient with the reference evapotranspiration on day i results in the crop evapotranspiration [mm/day] [59]. Extending this equation to include irrigation and precipitation results in a water balance model for each day i and pixel (x,y) [mm/day].

For UAV data:

$$WB_{i,xy} = -ETrefi \times 1.49 \times \left(2.13 \times NDVI_{UAV}^3 - 3.79 \times NDVI_{UAV}^2 + 2.75 \times NDVI_{UAV} - 0.1\right) - 0.22 \quad (11)$$

For PlanetScope data:

$$WB_{i,xy} = -ETrefi \times 1.49 \times (-9.07 \times NDVI_{Plan}^4 + 21.72 \times NDVI_{Plan}^3 - 18.75 \times NDVI_{Plan}^2 + 7.77 \times NDVI_{Plan} - 0.82) - 0.22 \quad (12)$$

For Sentinel-2 data:

$$WB_{i,xy} = -ETrefi \times 1.49 \times \left(-0.99 \times NDVI_{S2}^2 + 1.84 \times NDVI_{S2} - 0.0022\right) - 0.22 \quad (13)$$

In a last step, daily data can be summed up to a certain day n [mm] to obtain the cumulated water balance for every pixel.

For UAV data:

$$WB_{n,xy} = \sum_{i=1}^{n} (-ETrefi \times 1.49 \times (2.13 \times NDVI_{UAV}^3 - 3.79 \times NDVI_{UAV}^2 + 2.75 \times NDVI_{UAV} - 0.1) - 0.22) \quad (14)$$

For Planet data:

$$WB_{n,xy} = \sum_{i=1}^{n} (-ETrefi \times 1.49 \times (-9.07 \times NDVI_{Plan}^4 + 21.72 \times NDVI_{Plan}^3 - 18.75 \times NDVI_{Plan}^2 + 7.77 \times NDVI_{Plan} - 0.82) - 0.22) \quad (15)$$

For Sentinel-2 data:

$$WB_{n,xy} = \sum_{i=1}^{n} \left(-ETrefi \times 1.49 * \left(-0.99 \times NDVI_{S2}^2 + 1.84 \times NDVI_{S2} - 0.0022\right) - 0.22\right) \quad (16)$$

3.9. Summary of Model Results

All in all, the results can be presented as maps of *NDVI*, crop coefficient, cumulative crop evapotranspiration [mm], cumulative precipitation [mm], cumulative irrigation [mm], and cumulative water balance [mm] across the entire area of interest (AOI) for a given day (Figure 13, here DOY = 187 and DAP = 78, resp.), as well as a temporal progression for four specific points of interest (POI). Results showing different years and modifications can be found in the Appendix A Figures A1–A12.

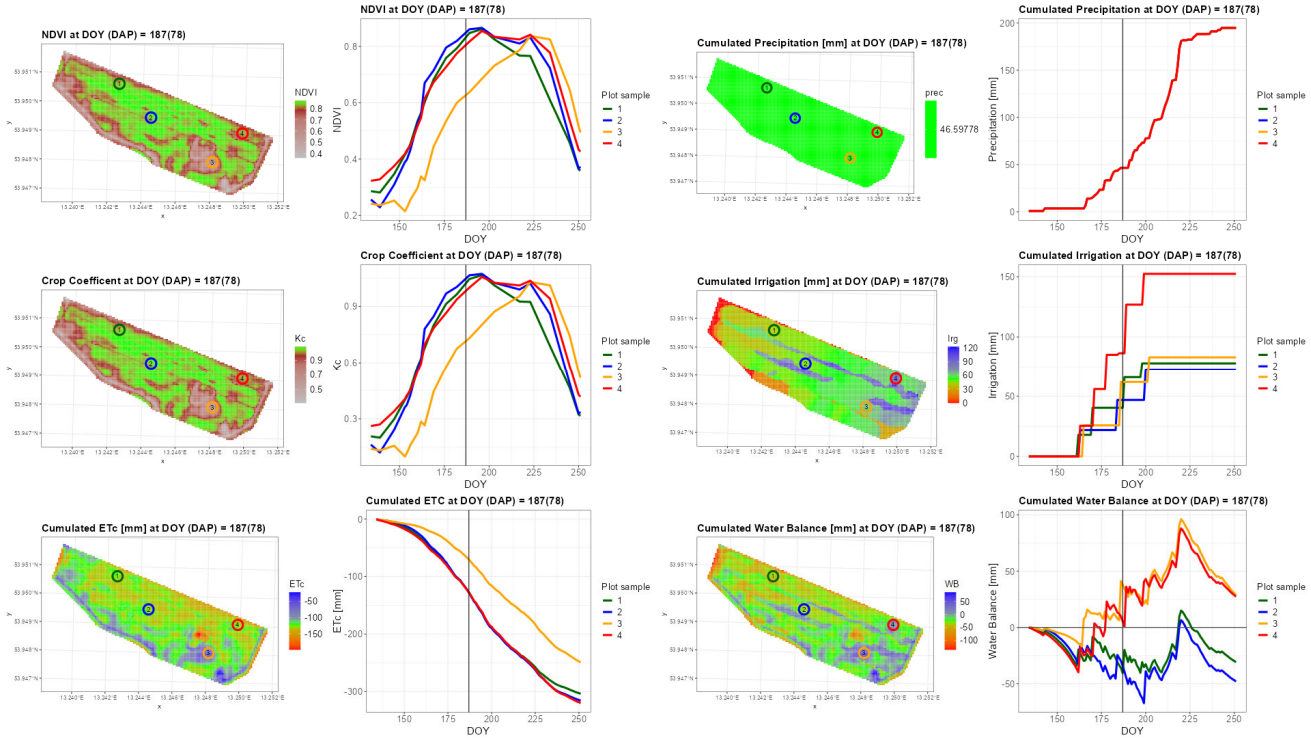

Figure 13. Model output for a sample date in 2023 (DOY = 187, DAP = 78) with RADOLAN-WR and ET_{ref} by German Weather Service. Shown is the spatial distribution of NDVI (**upper left**), crop coefficient (**middle left**), cumulated crop evapotranspiration [mm] (**lower left**), cumulated precipitation [mm] (**upper right**), cumulated irrigation [mm] (**middle right**), and cumulated water balance [mm] (**lower right**), each together with their temporal progression of four sample points on their right-hand side according to the colors shown in the map. As NDVI and *Kc* show a similar pattern due to their correlation, the orange-colored POI shows a different pattern with a slower decline regarding cumulated evapotranspiration, i.e., the loss of water is lower than on the other POIs. For all the four POIs, precipitation is similar. Irrigation shows that the red-colored POI achieved more irrigation than the other POIs due to a malfunction and an additional irrigation event. The cumulated water balances show a similar pattern of red- and orange-colored POIs due to the higher irrigation in the red-colored POI and the lower loss of water in the orange-colored POI. Here, the balance is positive across the last 2/3 of the vegetation period, whereas the blue- and green-colored POIs show a similar general pattern, although being almost all the time in a negative water balance level due to lower irrigation and a higher loss of water by evapotranspiration. So, water could have been saved by less irrigation on the red- and orange-colored POIs and could have spent on blue- and green-colored POIs instead.

4. Discussion

4.1. Objective and Success of the Model

The aim of the experiment was to develop a remote sensing-based model that provides farmers with high-resolution spatial and temporal assistance for irrigation management of starch potatoes, without overly restricting their own judgment through specific recommendations. The approach of choice was to generate maps from the model that enables farmers to identify specific sub-areas requiring additional irrigation due to deficits, as well as areas where reduced irrigation is sufficient, thus saving both water and the electrical energy required for pumping. In addition, the model was designed to be relatively easy to use, relying on a limited number of data sources and cost-effective solutions to facilitate adoption in agricultural practice. This goal was successfully achieved. The achieved spatial resolution of up to 5 m even exceeds the feasible precision with drum sprinklers; however, this was intentional to ensure adaptability to higher-resolution irrigation methods such as

drip or subsurface irrigation, thereby broadening the model's applicability. Discussions with farmers in northeastern and Central Germany indicated that sprinkler irrigation remains the preferred method due to its flexibility and lower labor requirements for setup and removal compared to alternative systems. Nonetheless, a shift in perspective is already underway. Rising energy costs and, in some regions, increasing water extraction fees are raising overall irrigation expenses, making more water-efficient methods—despite their higher labor demands and disadvantages—more attractive. Considering ongoing climate change, a shift toward more water-efficient irrigation methods appears likely, which is also highly desirable from an ecological perspective.

4.2. NDVI Data Sources

The model can incorporate three different *NDVI* data sources: DJI Phantom 4 Multispectral (UAV), Sentinel-2, and PlanetScope. Regarding UAV use, it became evident that deployment is highly time-consuming. Key limiting factors include travel time, the relatively low area coverage of quadcopter drones, and the high number of batteries required (approximately three batteries per 24 ha). These aspects contribute to operational costs that may initially discourage farmers from using UAVs, as they outweigh both the economic savings and ecological benefits of resource conservation achieved through the model. Detailed cost analyses related to UAV use are provided in Gütschow and Fuchs [65]. Future developments toward fully automated UAV systems ("drone-in-a-box") are expected (refs. [66,67], https://www.american-robotics.com/optimus-system, www.dronehub.ai; accessed 6 December 2024). Unlike the current UAV used in this study, which relies on predefined autopilot flight plans, these systems may operate fully autonomously, including automated battery recharging at docking stations. Furthermore, artificial intelligence may take over flight planning [68]. Another cost driver is the photogrammetry software Pix4Dmapper (versions 4.6.0 and later 4.8.0), which was used to process raw imagery into orthomosaics. However, substantial progress has recently been achieved with the open-source software OpenDroneMap (ODM, https://www.opendronemap.org/odm/, accessed 6 December 2024 [69]), which now delivers high-quality results. This offers opportunities for extending the model, as orthomosaics can be created via scripting with ODM rather than Pix4Dmapper, making the workflow more accessible and reproducible. Overall, our findings are consistent with the current literature on the usability, advantages, and limitations of UAVs and ground stations: while satellite resolution is sufficient for tracking and planning irrigation, temporal availability is restricted by cloud cover. UAVs, by contrast, provide greater flexibility for on-demand acquisitions and higher temporal frequency [17,69–72].

Sentinel-2 data, by comparison, are significantly more cost-effective, as they are freely available (https://dataspace.copernicus.eu, accessed 9 December 2024), while offering sufficient spatial resolution (native 10 m, rescalable to 5 m). The DEMMIN study area benefits from regular coverage by both Sentinel-2A and Sentinel-2B, yielding a theoretical revisit of twice per week. However, persistent cloud cover reduces the number of usable images to only 16 across the three vegetation periods (2021: 6, 2022: 4, 2023: 6, each <10% cloud cover). This limited dataset weakens the model's foundation. Moreover, correlation with ground station *NDVI* revealed a data gap in the range $0.6 < NDVI_{\text{Sentinel-2}} < 0.8$, which is particularly critical because PlanetScope and UAV data indicate an inflection point in this range, making a third-degree polynomial necessary. In practice, applying the model with only 4–6 images per vegetation period is problematic, as linear interpolation of *NDVI* between scenes results in the loss of important curve details, thereby reducing reliability. Cloud detection algorithms may increase the number of usable images slightly [73], but the study area's proximity to the Baltic Sea makes frequent cloud cover unavoidable.

Application in regions with less persistent cloudiness may therefore be more effective, even at the cost of lower revisit frequency.

As a third *NDVI* source, we used PlanetScope Level 3B data, calibrated to Sentinel-2 to ensure comparability and facilitate integration. Owing to the large number of PlanetScope CubeSats, revisit frequency was significantly higher, ranging from one to two acquisitions per day over the study area during the vegetation periods [74]. Although PlanetScope imagery provides high temporal resolution, it is inherently affected by radiometric and spatial inconsistencies due to its multi-satellite constellation [75–78]. While the normalized construction of *NDVI* generally confers robustness, variations in viewing geometry, sensor spectral response, and atmospheric conditions can still impact the stability of the index. Regression-based calibration with ground sensors, as applied in this study, helps mitigate these effects; however, residual variability across different PlanetScope acquisitions indicates that sensor inconsistencies remain a source of uncertainty. A clearer understanding of these limitations is essential to ensure methodological transparency and to improve the transferability of *NDVI*-based crop coefficient models to other sites and conditions. Since all acquisitions from the different PlanetScope satellites were included in the correlation between *NDVI* derived from Arable Mark 2 and PlanetScope-based *NDVI*, deviations caused by radiometric differences between individual satellites, atmospheric disturbances, or spatial variability within a given year would be expected to appear as outliers. However, as no discernible pattern is observed in a residual analysis, the unexplained variance attributable to individual satellites and spatial differences is small compared to the explained variance. This is also reflected in the model performance metrics (RSE = 0.05, R^2 = 0.95 ***). However, it should be noted that, particularly when applying the models to other regions, atmospheric disturbances, variations in viewing geometry, and differences in geomorphology may result in divergent outcomes. The GFZ Potsdam received PlanetScope data for research purposes within the AgriSens-DEMMIN 4.0 project through the Federal Agency for Cartography and Geodesy. However, for commercially oriented applications, the data must be purchased, which introduces costs that could restrict its applicability for the model and, consequently, its adoption in agricultural practice.

While UAV, PlanetScope, and Sentinel-2 data were harmonized at a common 5 m scale in this study, the high-resolution spatial information provided by UAV and PlanetScope imagery was inevitably reduced. The effects of scaling and resampling, which may lead to information loss at the precision-farming scale, were carefully evaluated. After testing several approaches, bilinear interpolation using 3 × 3 cell windows was selected. Alternative interpolation techniques introduced artifacts, such as artificial positive or negative hotspots in the modeled water balance that were not supported by observations. Although bilinear interpolation still produces mixed pixels, it proved to be the most robust option. Furthermore, the sprinkler system used in the experiments irrigated within a radius of 36 m, encompassing a relatively large number of pixels. Consequently, even when localized differences in water demand were identified, pixel-level adjustment was not feasible. The underlying model of this study has been published as the open-source software, WaterBalanceR (version 0.1.15, https://doi.org/10.5281/zenodo.15046338, accessed on 11 July 2025), with a corresponding paper currently under review in the Journal of Open Source Software. This software enables users to set the spatial resolution to as fine as one meter, allowing for high-resolution applications in cases where irrigation systems can support such precision.

4.3. Reference Evapotranspiration

The model can process reference evapotranspiration data, which can either be freely accessed from the German Weather Service (DWD) via its CDC portal [52] or provided

by installed Arable Mark 2 stations, and potentially their successors, the Arable Mark 3 stations.

Both data sources show similar trends; however, on warm days, the Mark 2 stations report higher peak values than those generated by the DWD. This discrepancy can be attributed to differences in spatial resolution and calculation methods: ground stations directly measure all parameters required to calculate ET_{ref} on-site, whereas DWD relies on data from its climate stations, interpolated at a spatial resolution of 1 km.

This introduces two key issues:

- Interpolation gaps: Due to the distance between the climate stations, certain localized areas may not be captured during interpolation.
- Mixed pixels: At the 1 km scale, pixels may include heterogeneous land cover (e.g., cropland, forests, meadows, or roads). For instance, elevated field temperatures that drive ET_{ref} may be averaged out by cooler forested areas within the same pixel. The same applies to other parameters required for ET_{ref}.

A second factor is the difference in calculation methods. While both DWD and Arable calculate ET_{ref} following FAO Paper 56 [59], Arable reportedly applies an AI-based system for computation and correction. However, details of this process are not publicly available.

DWD data is freely available Germany-wide but offers limited resolution, potentially missing fine-scale variability. Arable data provides higher spatial detail but requires purchasing or leasing stations, which introduces additional costs.

4.4. Weather Radar and Precipitation

In this study, we also used freely available precipitation data from the German Weather Service (DWD), accessible via its CDC portal [52], with a spatial resolution of 1 km. We compared the RADOLAN product with X-band radar data, which provides a finer resolution of 100 m [54]. While the higher resolution improves the detection of intra-site precipitation variability that is lost in RADOLAN due to its coarse resolution, the effectiveness of X-band radar over the study sites was limited. Specifically, radar beams were deflected by tree canopies, preventing accurate precipitation detection directly above the fields. Local measurement devices further revealed substantial variability in precipitation at the sub-field scale, highlighting the importance of higher-resolution monitoring. Although the X-band radar in Neubrandenburg (Mecklenburg–Western Pomerania) covers a wide area with an effective radius of 50 km, it remains restricted to a local perspective as it is operated as a research radar. A potential compromise is the use of hh-data with a spatial resolution of 250 m, which is currently being tested and refined by the DWD in cooperation with GFZ Potsdam.

4.5. Sites, Design, and Irrigation

The experiment began in 2021 with the observation of one irrigated track as the treatment and an adjacent track as the control. It became evident that irrigation could only be conducted with variance from the target irrigation amount. This variability was caused partly by the large sprinkler radius (40 m) and partly by the sprinkler's sensitivity to even small fluctuations in water pressure (e.g., a 0.5 bar change can alter precipitation height by up to 2 mm [51]), as well as by sprinkler speed, field morphology, and soil conditions.

Variance was confirmed both through thermal UAV observations (Parrot Anafi Thermal) and Raindancer log data. However, monitoring only a single irrigated track naturally covered only a small sub-area, which limited the applicability of satellite data due to their coarser spatial resolution.

For this reason, an entire neighboring field was monitored in 2022, which proved successful and was continued in 2023. In 2023, however, the sensor setup was slightly

modified to meet the requirements of the Eddy Covariance System. This adjustment did not affect data processing or model training, as the devices were still distributed across a wide area to ensure extensive sampling.

4.6. Conclusions and Outlook

This study confirms (1) a strong correlation between *NDVI* and crop coefficient (*Kc*) values for starch potato, derived from Arable Mark 2 ground station data (Equation (4), $R^2 = 0.999$, $F_{(1,1328)} = 1{,}264{,}000$, $p < 0.001$, n = 1330, RSE = 0.02). (2) Together with cross-calibration of *NDVI* from Remote Sensing Sources, including DJI Phantom 4 Multispectral UAV (Equation (5), $R^2 = 0.95$, $F_{(3,102)} = 713.7$, $p < 0.001$, n = 106, RSE = 0.04), PlanetScope satellite data (Equation (7), $R^2 = 0.95$, $F_{(4,190)} = 905.98$, $p < 0.001$, n = 195, RSE = 0.05), and Sentinel-2 satellite data (Equation (9), $R^2 = 0.97$, $F_{(2,28)} = 397.97$, $p < 0.001$, n = 31, RSE = 0.04), this study successfully demonstrates the development of a high-resolution, *NDVI*-driven, crop coefficient-based water balance model. These two key outcomes ensure consistent *NDVI* estimates while demonstrating the model's reliability and versatility in capturing intra-field heterogeneity and enabling robust estimation of daily crop coefficient, evapotranspiration, and water balance across scales.

From a methodological perspective, the integration and cross-calibration of in situ and multi-source remote sensing data highlights the model's potential for transferability to other crops, sites, or sensor configurations. Practically, the approach provides a valuable basis for precision irrigation planning, supporting sustainable water use by enabling farmers to make data-driven decisions that effectively reduce water and energy consumption.

Nevertheless, operational constraints such as the cost and logistical demands of UAV deployment, as well as cloud-related limitations of Sentinel-2, underline the importance of complementary data sources like PlanetScope. Further advancements in automated UAV systems and the adoption of open-source software can significantly reduce costs and improve model accessibility for practical applications. Looking ahead, further development should focus on adapting the model to diverse climatic and soil conditions, integrating it with water-efficient irrigation technologies, and coupling it with AI-based real-time analytics to enhance adaptability and scalability.

Overall, this work provides a consistent and scalable *NDVI*-based framework for water balance modeling in agriculture, laying a foundation for more efficient and sustainable resource management in the context of increasing water scarcity and climate change.

Author Contributions: T.P., data curation, formal analysis, investigation, methodology, software, resources, validation, visualization, writing—original draft. M.K., supervision, funding acquisition, project administration, writing—review and editing. S.I., supervision, funding acquisition, project administration, resources. C.C., supervision, funding acquisition, project administration, resources, writing—review and editing. J.L.W., investigation. J.P., supervision, investigation. All authors have read and agreed to the published version of the manuscript.

Funding: This research was funded by the Federal Ministry of Food and Agriculture (BMEL) based on a decision of the Parliament of the Federal Republic of Germany. The Federal Office for Agriculture and Food (BLE) supplies coordinating support for digitalization in agriculture as funding organization, grant number: FKZ 28DE114A18 and 28DE114A22.

Data Availability Statement: According data of the whole experiment will be published soon in a separate publication.

Acknowledgments: We acknowledge the financial support of the Open Access Publication Fund of the GFZ Helmholtz Centre for Geosciences as well as our partner farm, the Bentziner Ackerbau GmbH and Falk Böttcher from German Weather Service for consistently valuable advice.

Conflicts of Interest: The authors declare no conflicts of interest.

Appendix A

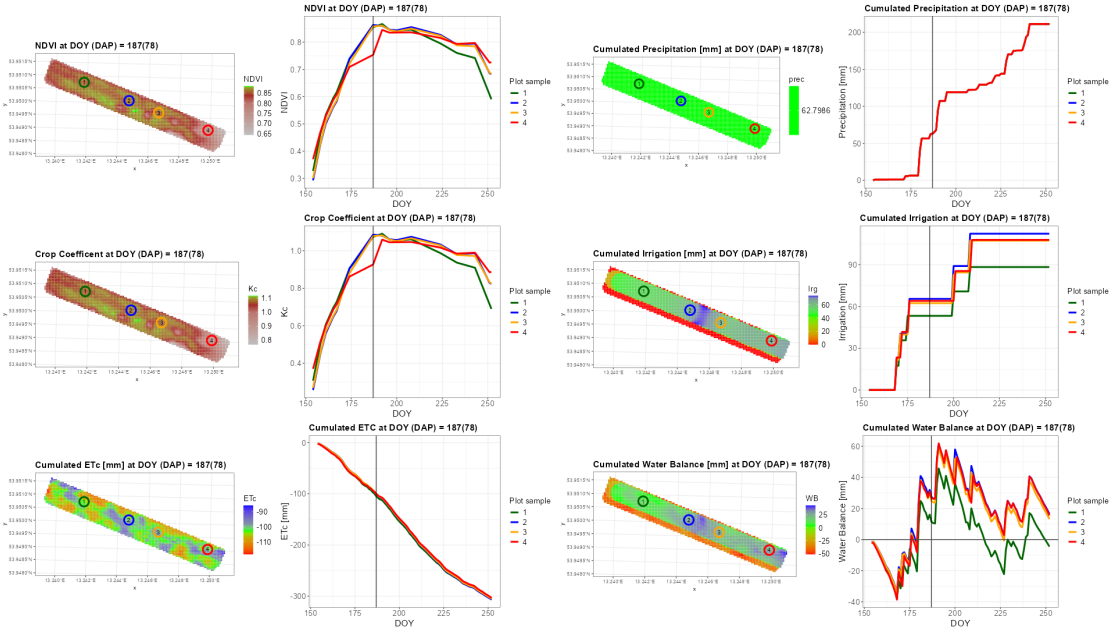

Figure A1. Results showing *NDVI*, crop coefficient, cumulated *ETc*, precipitation, irrigation, and cumulated water balance for doy = 187 (dap = 78) in 2021 using both UAV and PlanetScope data. Shown is the spatial distribution of *NDVI* (**upper left**), crop coefficient (**middle left**), cumulated crop evapotranspiration [mm] (**lower left**), cumulated precipitation [mm] (**upper right**), cumulated irrigation [mm] (**middle right**), and cumulated water balance [mm] (**lower right**), each together with their temporal progression of four sample points on their right-hand side according to the colors shown in the map.

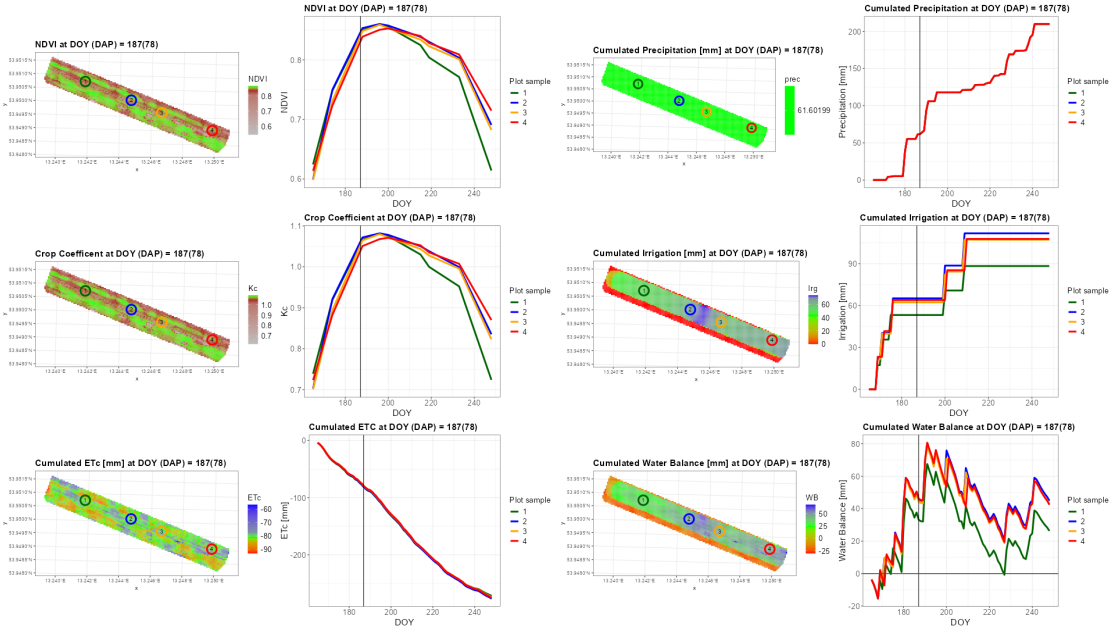

Figure A2. Results showing *NDVI*, crop coefficient, cumulated *ETc*, precipitation, irrigation, and cumulated water balance for doy = 187 (dap = 78) in 2021 using only UAV data. Shown is the spatial distribution of *NDVI* (**upper left**), crop coefficient (**middle left**), cumulated crop evapotranspiration [mm] (**lower left**), cumulated precipitation [mm] (**upper right**), cumulated irrigation [mm] (**middle right**), and cumulated water balance [mm] (**lower right**), each together with their temporal progression of four sample points on their right-hand side according to the colors shown in the map.

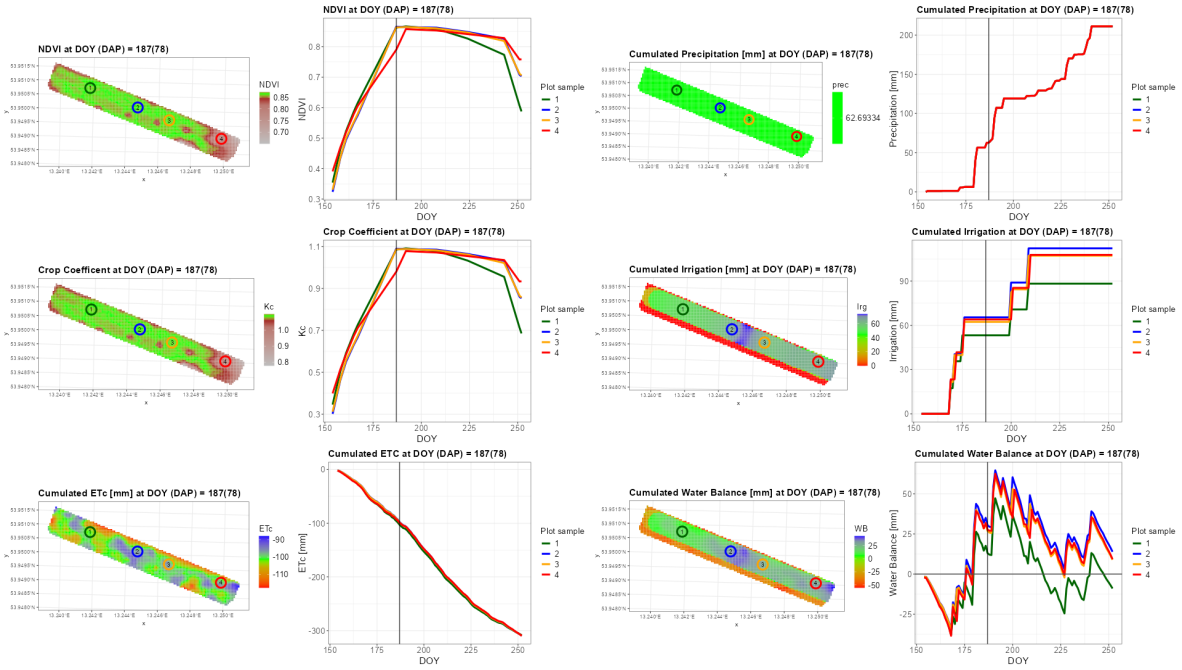

Figure A3. Results showing *NDVI*, crop coefficient, cumulated *ETc*, precipitation, irrigation, and cumulated water balance for doy = 187 (dap = 78) in 2021 using PlanetScope data. Shown is the spatial distribution of *NDVI* (**upper left**), crop coefficient (**middle left**), cumulated crop evapotranspiration [mm] (**lower left**), cumulated precipitation [mm] (**upper right**), cumulated irrigation [mm] (**middle right**), and cumulated water balance [mm] (**lower right**), each together with their temporal progression of four sample points on their right-hand side according to the colors shown in the map.

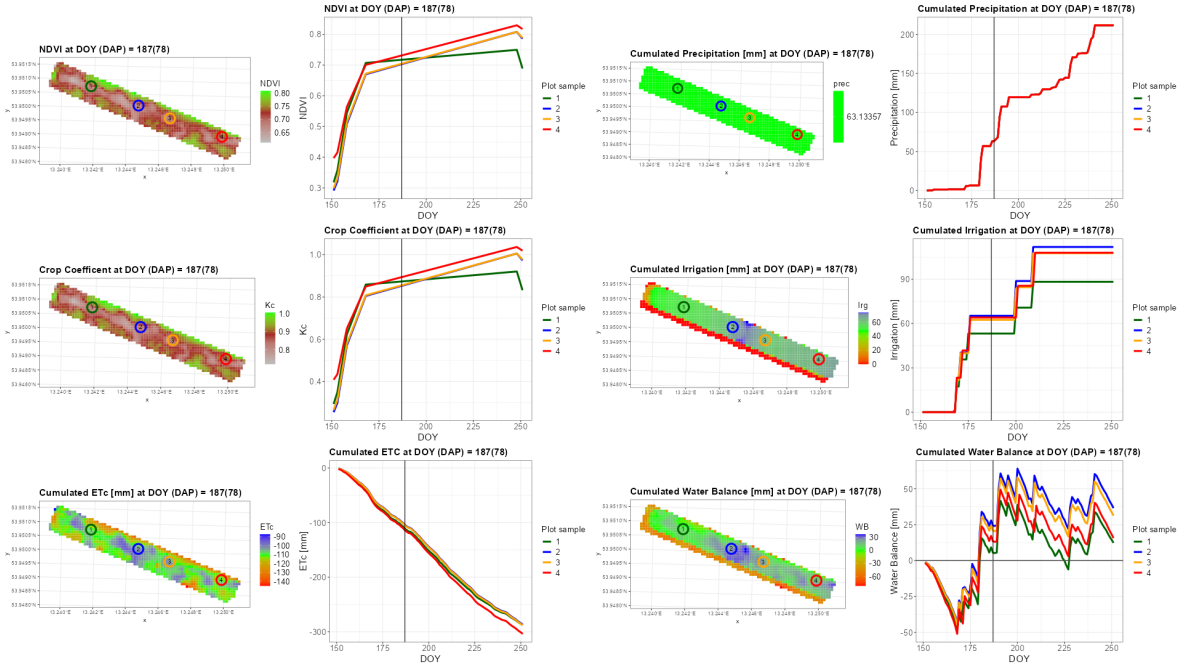

Figure A4. Results showing *NDVI*, crop coefficient, cumulated *ETc*, precipitation, irrigation, and cumulated water balance for doy = 187 (dap = 78) in 2021 using Sentinel-2 data. Shown is the spatial distribution of *NDVI* (**upper left**), crop coefficient (**middle left**), cumulated crop evapotranspiration [mm] (**lower left**), cumulated precipitation [mm] (**upper right**), cumulated irrigation [mm] (**middle right**), and cumulated water balance [mm] (**lower right**), each together with their temporal progression of four sample points on their right-hand side according to the colors shown in the map.

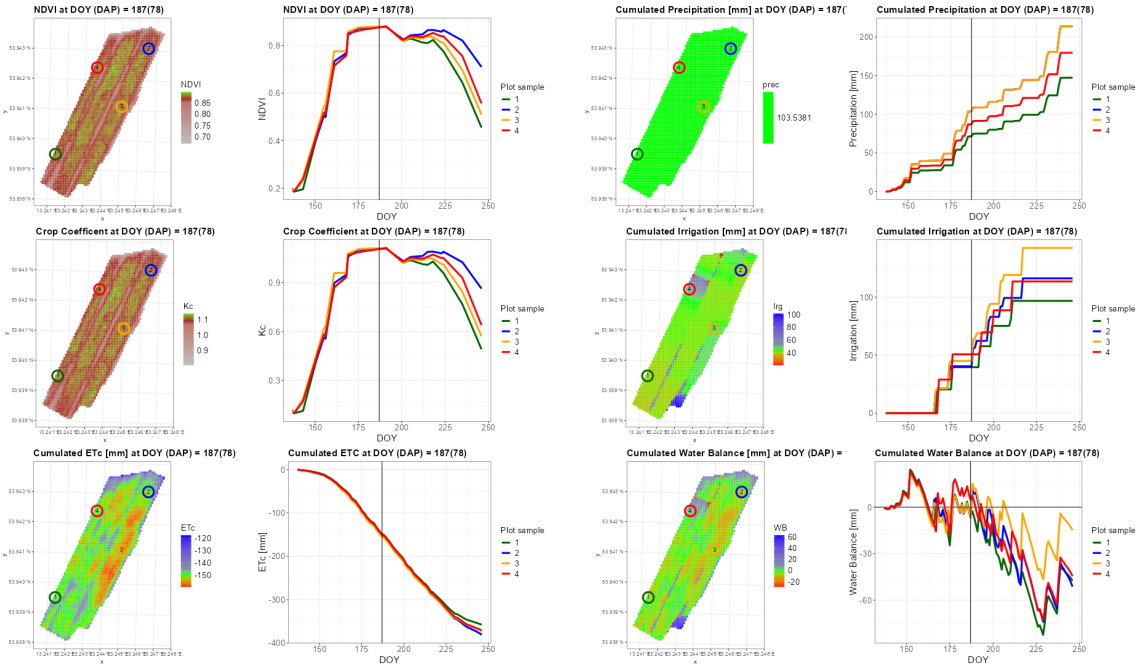

Figure A5. Results showing *NDVI*, crop coefficient, cumulated *ETc*, precipitation, irrigation, and cumulated water balance for doy = 187 (dap = 78) in 2022 using both UAV and PlanetScope data. Shown is the spatial distribution of *NDVI* (**upper left**), crop coefficient (**middle left**), cumulated crop evapotranspiration [mm] (**lower left**), cumulated precipitation [mm] (**upper right**), cumulated irrigation [mm] (**middle right**), and cumulated water balance [mm] (**lower right**), each together with their temporal progression of four sample points on their right-hand side according to the colors shown in the map.

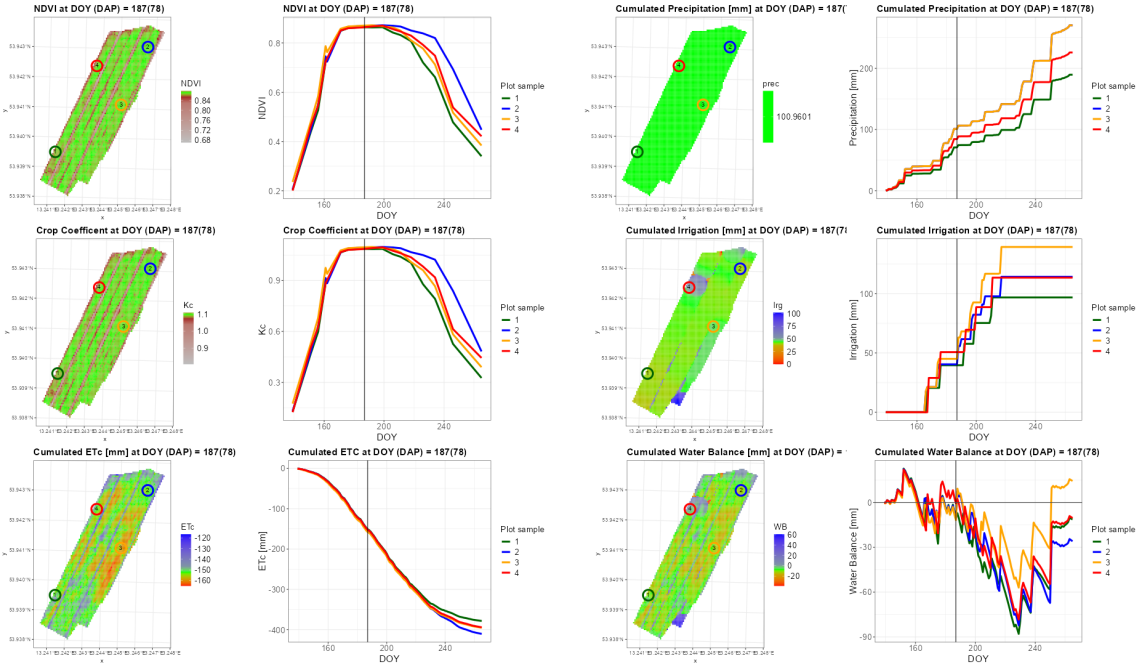

Figure A6. Results showing *NDVI*, crop coefficient, cumulated *ETc*, precipitation, irrigation, and cumulated water balance for doy = 187 (dap = 78) in 2022 using UAV data. Shown is the spatial distribution of *NDVI* (**upper left**), crop coefficient (**middle left**), cumulated crop evapotranspiration [mm] (**lower left**), cumulated precipitation [mm] (**upper right**), cumulated irrigation [mm] (**middle right**), and cumulated water balance [mm] (**lower right**), each together with their temporal progression of four sample points on their right-hand side according to the colors shown in the map.

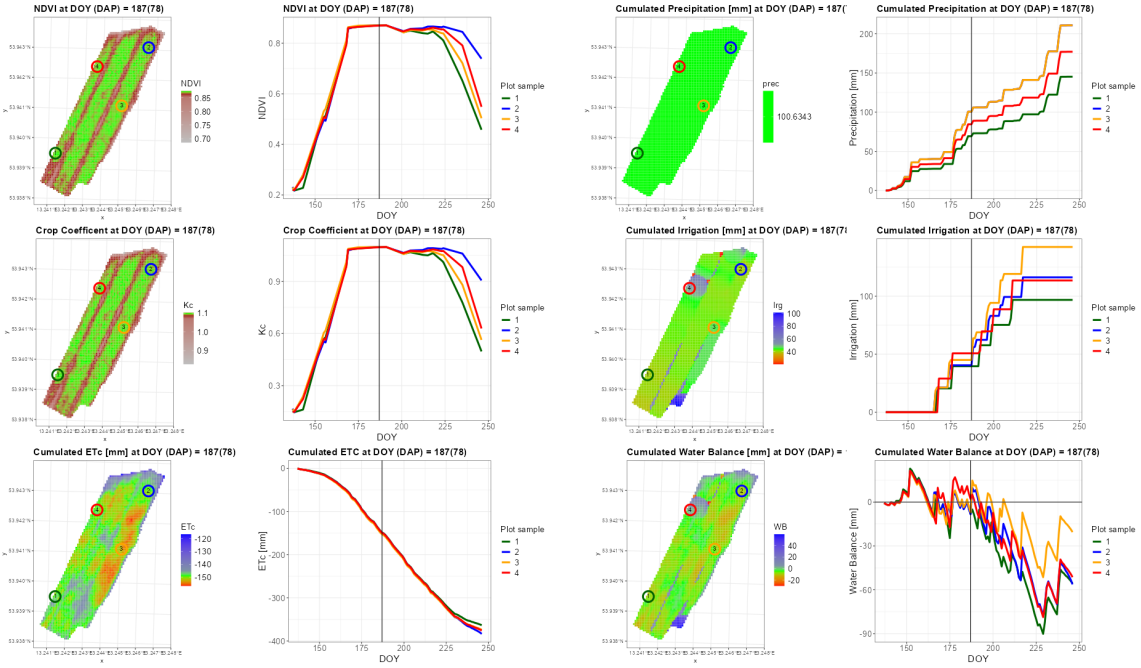

Figure A7. Results showing *NDVI*, crop coefficient, cumulated *ETc*, precipitation, irrigation, and cumulated water balance for doy = 187 (dap = 78) in 2022 using PlanetScope data. Shown is the spatial distribution of *NDVI* (**upper left**), crop coefficient (**middle left**), cumulated crop evapotranspiration [mm] (**lower left**), cumulated precipitation [mm] (**upper right**), cumulated irrigation [mm] (**middle right**), and cumulated water balance [mm] (**lower right**), each together with their temporal progression of four sample points on their right-hand side according to the colors shown in the map.

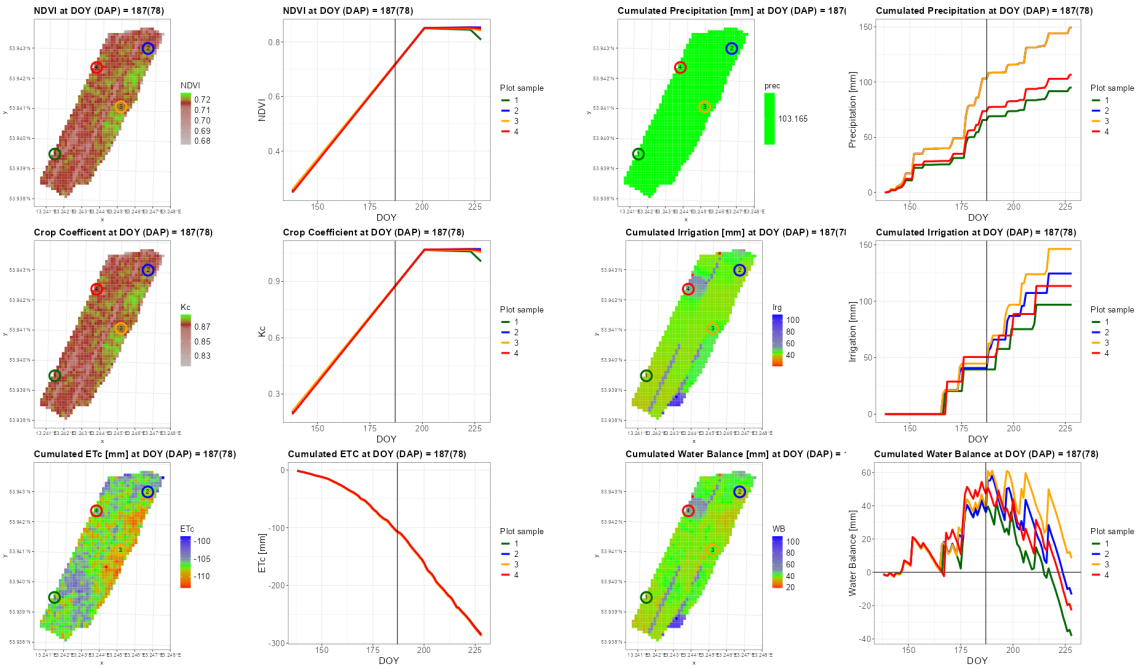

Figure A8. Results showing *NDVI*, crop coefficient, cumulated *ETc*, precipitation, irrigation, and cumulated water balance for doy = 187 (dap = 78) in 2022 using Sentinel-2 data. Shown is the spatial distribution of *NDVI* (**upper left**), crop coefficient (**middle left**), cumulated crop evapotranspiration [mm] (**lower left**), cumulated precipitation [mm] (**upper right**), cumulated irrigation [mm] (**middle right**), and cumulated water balance [mm] (**lower right**), each together with their temporal progression of four sample points on their right-hand side according to the colors shown in the map.

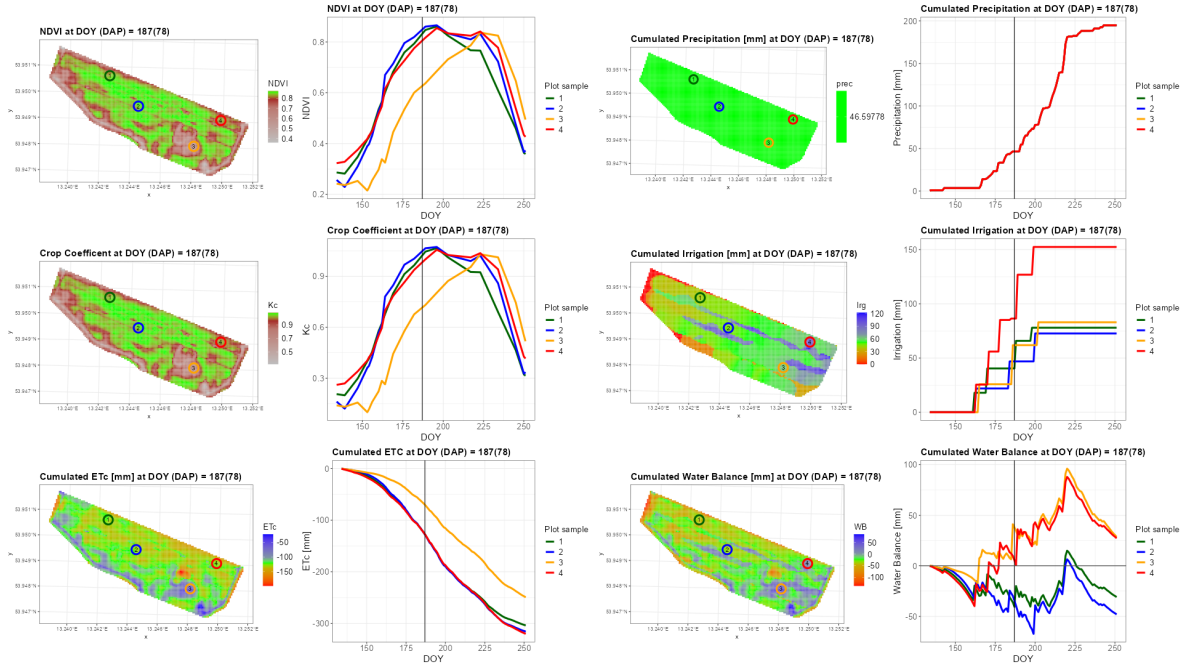

Figure A9. Results showing *NDVI*, crop coefficient, cumulated *ETc*, precipitation, irrigation, and cumulated water balance for doy = 187 (dap = 78) in 2023 using both UAV and PlanetScope data. Shown is the spatial distribution of *NDVI* (**upper left**), crop coefficient (**middle left**), cumulated crop evapotranspiration [mm] (**lower left**), cumulated precipitation [mm] (**upper right**), cumulated irrigation [mm] (**middle right**), and cumulated water balance [mm] (**lower right**), each together with their temporal progression of four sample points on their right-hand side according to the colors shown in the map.

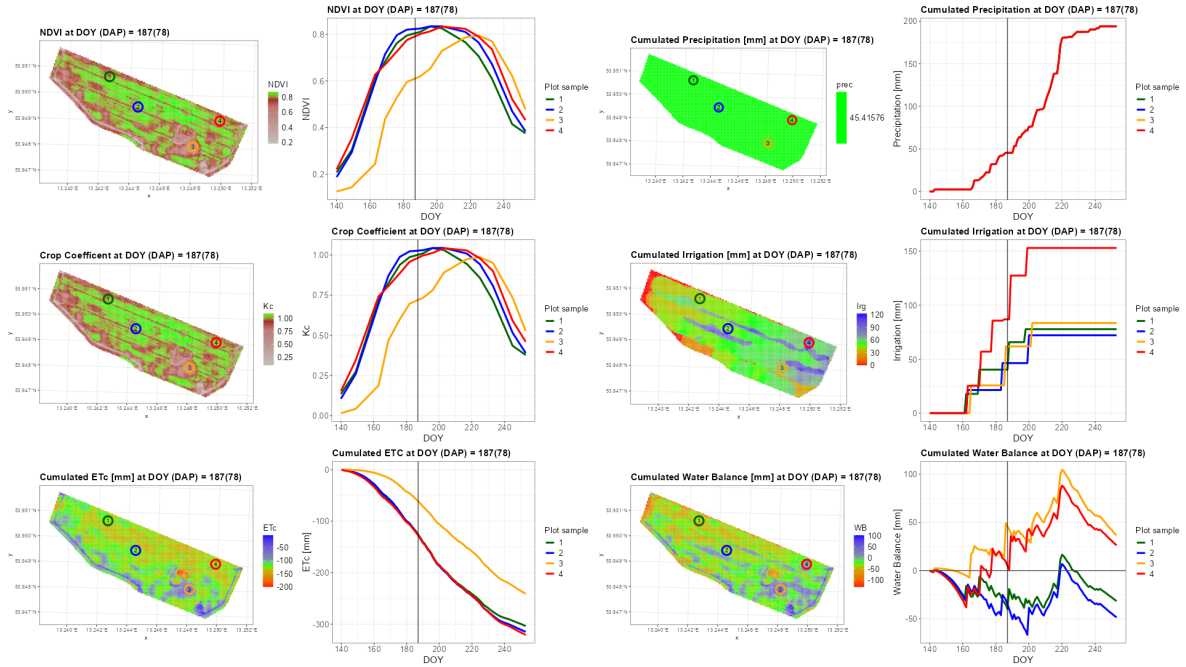

Figure A10. Results showing *NDVI*, crop coefficient, cumulated *ETc*, precipitation, irrigation, and cumulated water balance for doy = 187 (dap = 78) in 2023 using UAV data. Shown is the spatial distribution of *NDVI* (**upper left**), crop coefficient (**middle left**), cumulated crop evapotranspiration [mm] (**lower left**), cumulated precipitation [mm] (**upper right**), cumulated irrigation [mm] (**middle right**), and cumulated water balance [mm] (**lower right**), each together with their temporal progression of four sample points on their right-hand side according to the colors shown in the map.

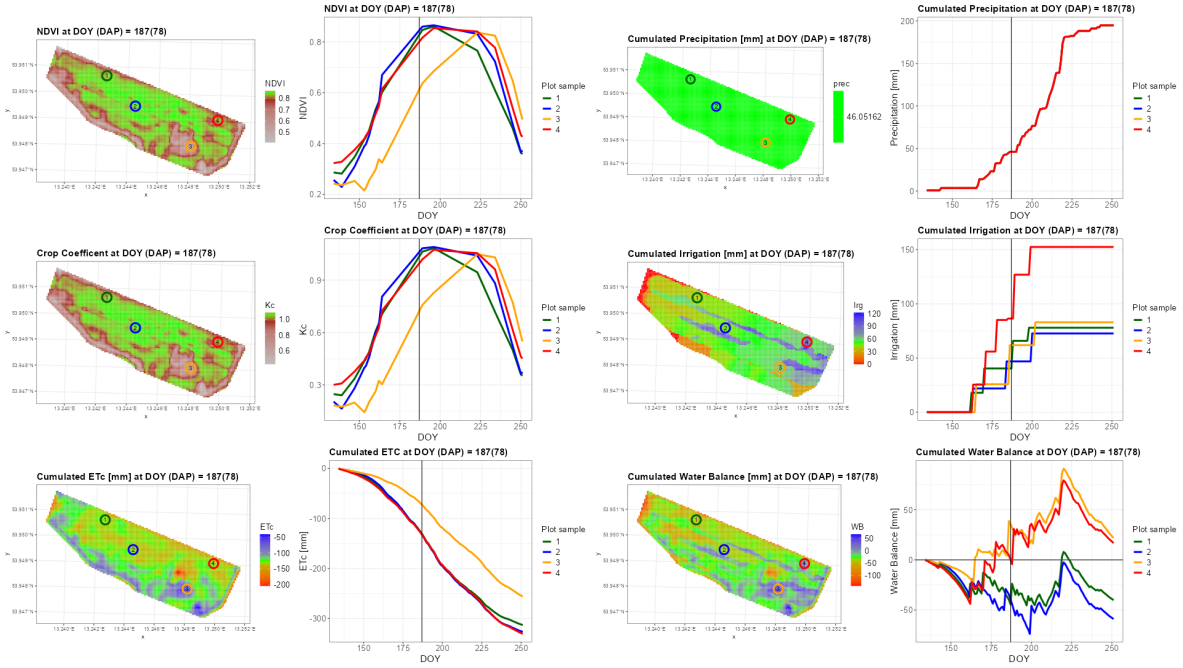

Figure A11. Results showing *NDVI*, crop coefficient, cumulated *ETc*, precipitation, irrigation, and cumulated water balance for doy = 187 (dap = 78) in 2023 using PlanetScope data. Shown is the spatial distribution of *NDVI* (**upper left**), crop coefficient (**middle left**), cumulated crop evapotranspiration [mm] (**lower left**), cumulated precipitation [mm] (**upper right**), cumulated irrigation [mm] (**middle right**), and cumulated water balance [mm] (**lower right**), each together with their temporal progression of four sample points on their right-hand side according to the colors shown in the map.

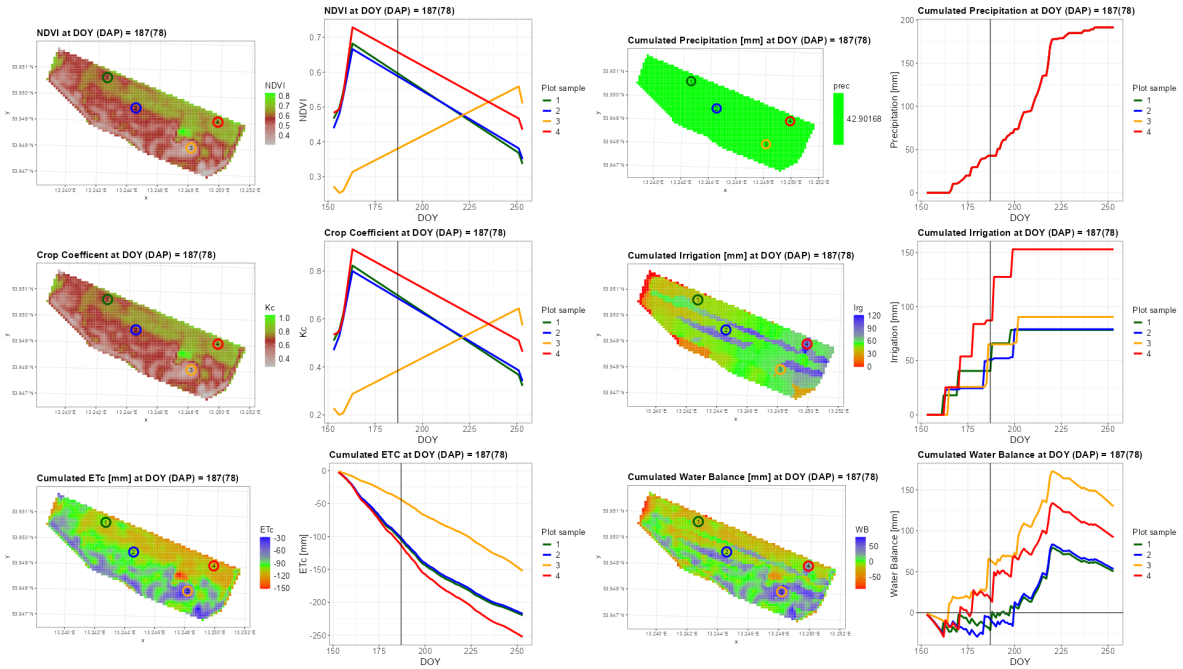

Figure A12. Results showing *NDVI*, crop coefficient, cumulated *ETc*, precipitation, irrigation, and cumulated water balance for doy = 187 (dap = 78) in 2023 using Sentinel-2 data. Shown is the spatial distribution of *NDVI* (**upper left**), crop coefficient (**middle left**), cumulated crop evapotranspiration [mm] (**lower left**), cumulated precipitation [mm] (**upper right**), cumulated irrigation [mm] (**middle right**), and cumulated water balance [mm] (**lower right**), each together with their temporal progression of four sample points on their right-hand side according to the colors shown in the map.

References

1. FAO. *World Food and Agriculture—Statistical Yearbook*; FAO: Rome, Italy, 2021. [CrossRef]
2. FAO; IFAD; UNICEF; WFP; WHO. *The State of Food Security and Nutrition in the World 2022*; FAO: Rome, Italy; IFAD: Rome, Italy; UNICEF: New York, NY, USA; WFP: Rome, Italy; WHO: Geneva, Switzerland, 2022. [CrossRef]
3. van Vuuren, D.P.; Edmonds, J.A.; Kainuma, M.; Riahi, K.; Weyant, J. A Special Issue on the RCPs. *Clim. Change* **2011**, *109*, 1. [CrossRef]
4. Egerer, S.; Puente, A.F.; Peichl, M.; Rakovec, O.; Samaniego, L.; Schneider, U.A. Limited Potential of Irrigation to Prevent Potato Yield Losses in Germany under Climate Change. *Agric. Syst.* **2023**, *207*, 103633. [CrossRef]
5. Riediger, J.; Breckling, B.; Nuske, R.S.; Schröder, W. Will Climate Change Increase Irrigation Requirements in Agriculture of Central Europe? A Simulation Study for Northern Germany. *Environ. Sci. Eur.* **2014**, *26*, 18. [CrossRef] [PubMed]
6. Goffart, J.-P.; Haverkort, A.; Storey, M.; Haase, N.; Martin, M.; Lebrun, P.; Ryckmans, D.; Florins, D.; Demeulemeester, K. Potato Production in Northwestern Europe (Germany, France, the Netherlands, United Kingdom, Belgium): Characteristics, Issues, Challenges and Opportunities. *Potato Res.* **2022**, *65*, 503–547. [CrossRef] [PubMed]
7. Supit, I.; van Diepen, C.A.; de Wit, A.J.W.; Kabat, P.; Baruth, B.; Ludwig, F. Recent Changes in the Climatic Yield Potential of Various Crops in Europe. *Agric. Syst.* **2010**, *103*, 683–694. [CrossRef]
8. Knežević, M.; Zivotić, L.; Čereković, N.; Topalović, A.; Koković, N.; Todorovic, M. Impact of Climate Change on Water Requirements and Growth of Potato in Different Climatic Zones of Montenegro. *J. Water Clim. Change* **2018**, *9*, 657–671. [CrossRef]
9. Scarpare, F.V.; Rajagopalan, K.; Liu, M.; Nelson, R.L.; Stöckle, C.O. Evapotranspiration of Irrigated Crops under Warming and Elevated Atmospheric CO_2: What Is the Direction of Change? *Atmosphere* **2022**, *13*, 163. [CrossRef]
10. Badr, M.A.; El-Tohamy, W.A.; Salman, S.R.; Gruda, N. Yield and Water Use Relationships of Potato under Different Timing and Severity of Water Stress. *Agric. Water Manag.* **2022**, *271*, 107793. [CrossRef]
11. Karam, F.; Amacha, N.; Fahed, S.; Asmar, T.E.; Domínguez, A. Response of Potato to Full and Deficit Irrigation under Semiarid Climate: Agronomic and Economic Implications. *Agric. Water Manag.* **2014**, *142*, 144–151. [CrossRef]
12. Crosby, T.W.; Wang, Y. Effects of Different Irrigation Management Practices on Potato (*Solanum tuberosum* L.). *Sustainability* **2021**, *13*, 187. [CrossRef]
13. Onder, S.; Caliskan, M.E.; Onder, D.; Caliskan, S. Different Irrigation Methods and Water Stress Effects on Potato Yield and Yield Components. *Agric. Water Manag.* **2005**, *73*, 73–86. [CrossRef]
14. Walker, W.R. *FAO Irrigation and Drainage Paper No. 45*; Food and Agriculture Organization of the United Nations: Rome, Italy, 1989; p. 45.
15. Deutscher Wetterdienst (DWD). AMBAV. Available online: https://opendata.dwd.de/climate_environment/CDC/derived_germany/soil/daily/recent/AMBAV.pdf (accessed on 11 July 2025).
16. Braden, H. Agrarmeteorologische Modelle des Wasser- und Energiehaushalts im Deutschen Wetterdienst. *Promet* **2012**, *38*, 11–19.
17. Sishodia, R.P.; Ray, R.L.; Singh, S.K. Applications of Remote Sensing in Precision Agriculture: A Review. *Remote Sens.* **2020**, *12*, 3136. [CrossRef]
18. Delgado, J.A.; Short, N.M.; Roberts, D.P.; Vandenberg, B. Big Data Analysis for Sustainable Agriculture on a Geospatial Cloud Framework. *Front. Sustain. Food Syst.* **2019**, *3*, 54. [CrossRef]
19. Georgi, C.; Spengler, D.; Itzerott, S.; Kleinschmit, B. Automatic Delineation Algorithm for Site-Specific Management Zones Based on Satellite Remote Sensing Data. *Precis. Agric.* **2018**, *19*, 684–707. [CrossRef]
20. Srinivasan, A. *Handbook of Precision Agriculture: Principles and Applications*; CRC Press: Boca Raton, FL, USA, 2006.
21. Pierce, F.J.; Nowak, P. Aspects of Precision Agriculture. In *Advances in Agronomy*; Sparks, D.L., Ed.; Academic Press: Cambridge, MA, USA, 1999; Volume 67, pp. 1–85. [CrossRef]
22. Lakhiar, I.A.; Yan, H.; Zhang, C.; Wang, G.; He, B.; Hao, B.; Han, Y.; Wang, B.; Bao, R.; Syed, T.N.; et al. A Review of Precision Irrigation Water-Saving Technology under Changing Climate for Enhancing Water Use Efficiency, Crop Yield, and Environmental Footprints. *Agriculture* **2024**, *14*, 1141. [CrossRef]
23. Bwambale, E.; Abagale, F.K.; Anornu, G.K. Smart Irrigation Monitoring and Control Strategies for Improving Water Use Efficiency in Precision Agriculture: A Review. *Agric. Water Manag.* **2022**, *260*, 107324. [CrossRef]
24. García, L.; Parra, L.; Jimenez, J.M.; Lloret, J.; Lorenz, P. IoT-Based Smart Irrigation Systems: An Overview on the Recent Trends on Sensors and IoT Systems for Irrigation in Precision Agriculture. *Sensors* **2020**, *20*, 1042. [CrossRef]
25. Meier, J.; Mauser, W. Irrigation Mapping at Different Spatial Scales: Areal Change with Resolution Explained by Landscape Metrics. *Remote Sens.* **2023**, *15*, 315. [CrossRef]
26. Monteleone, S.; Moraes, E.A.; Tondato de Faria, B.; Aquino Junior, P.T.; Maia, R.F.; Neto, A.T.; Toscano, A. Exploring the Adoption of Precision Agriculture for Irrigation in the Context of Agriculture 4.0: The Key Role of Internet of Things. *Sensors* **2020**, *20*, 7091. [CrossRef]
27. Dominique, C.; Seguin, B.; Olioso, A. Review on Estimation of Evapotranspiration from Remote Sensing Data: From Empirical to Numerical Modeling Approaches. *Irrig. Drain. Syst.* **2005**, *19*, 223–249. [CrossRef]

28. Maes, W.H.; Steppe, K. Estimating Evapotranspiration and Drought Stress with Ground-Based Thermal Remote Sensing in Agriculture: A Review. *J. Exp. Bot.* **2012**, *63*, 4671–4712. [CrossRef]
29. Atzberger, C. Correction: Atzberger, C. Advances in Remote Sensing of Agriculture: Context Description, Existing Operational Monitoring Systems and Major Information Needs. *Remote Sens.* **2013**, *5*, 949–981. [CrossRef]
30. Weiss, M.; Jacob, F.; Duveiller, G. Remote Sensing for Agricultural Applications: A Meta-Review. *Remote Sens. Environ.* **2020**, *236*, 111402. [CrossRef]
31. Mouniane, Y.; Chriqui, A.; El-Khadir, I.; Hbyaj, K.; El-Moustaqim, K.; Mezouara, M.; Zirari, M.; Mabrouki, J.; Hmouni, D. Impact of Remote Sensing on Irrigation Management in Precision Agriculture. In *Technical and Technological Solutions Towards a Sustainable Society and Circular Economy*; Mabrouki, J., Mourade, A., Eds.; Springer Nature: Cham, Switzerland, 2024; pp. 237–245. [CrossRef]
32. Mehedi, I.M.; Hanif, M.S.; Bilal, M.; Vellingiri, M.T.; Palaniswamy, T. Remote Sensing and Decision Support System Applications in Precision Agriculture: Challenges and Possibilities. *IEEE Access* **2024**, *12*, 44786–44798. [CrossRef]
33. Wang, J.; Wang, Y.; Li, G.; Qi, Z. Integration of Remote Sensing and Machine Learning for Precision Agriculture: A Comprehensive Perspective on Applications. *Agronomy* **2024**, *14*, 1975. [CrossRef]
34. Graf, L.; Bach, H.; Tiede, D. Semantic Segmentation of Sentinel-2 Imagery for Mapping Irrigation Center Pivots. *Remote Sens.* **2020**, *12*, 3937. [CrossRef]
35. Sharma, K.; Irmak, S.; Kukal, M. Propagation of Soil Moisture Sensing Uncertainty into Estimation of Total Soil Water, Evapotranspiration and Irrigation Decision-Making. *Agric. Water Manag.* **2021**, *243*, 106454. [CrossRef]
36. Stradiotti, P.; Dorigo, W.; Samaniego, L. Exploring the Relative Scale of Uncertainty in High-Resolution Soil Moisture Remote Sensing Products towards Model Integration. In Proceedings of the EGU General Assembly 2024, Vienna, Austria, 14–19 April 2024; p. EGU24-15519. [CrossRef]
37. Karamouz, M.; Alipour, R.S.; Roohinia, M.; Fereshtehpour, M. A Remote Sensing Driven Soil Moisture Estimator: Uncertain Downscaling With Geostatistically Based Use of Ancillary Data. *Water Resour. Res.* **2022**, *58*, e2022WR031946. [CrossRef]
38. Konkathi, P.; Karthikeyan, L. Error and Uncertainty Characterization of Soil Moisture and VOD Retrievals Obtained from L-Band SMAP Radiometer. *Remote Sens. Environ.* **2022**, *280*, 113146. [CrossRef]
39. Pasik, A.; Gruber, A.; Preimesberger, W.; De Santis, D.; Dorigo, W. Uncertainty Estimation for a New Exponential-Filter-Based Long-Term Root-Zone Soil Moisture Dataset from Copernicus Climate Change Service (C3S) Surface Observations. *Geosci. Model Dev.* **2023**, *16*, 4957–4976. [CrossRef]
40. Zhang, L.; Xue, Z.; Yu, J.; Yue, G. *Uncertainty Analysis of Remote Sensing Soil Moisture Estimation Over the Qinghai-Tibetan Plateau: Feature, Target, and Model*; IOS Press: Amsterdam, The Netherlands, 2024. [CrossRef]
41. Baroni, G.; Scheiffele, L.M.; Schrön, M.; Ingwersen, J.; Oswald, S.E. Uncertainty, Sensitivity and Improvements in Soil Moisture Estimation with Cosmic-Ray Neutron Sensing. *J. Hydrol.* **2018**, *564*, 873–887. [CrossRef]
42. Kraft, M.; Rolfes, J.; Meinardi, D.; Riedel, A. *Sensor Based Irrigation Management for Potatoes*; Thünen-Institut, Bundesforschungsinstitut für Ländliche Räume, Wald und Fischerei: Braunschweig, Germany, 2023. [CrossRef]
43. Ekinzog, E.K.; Schlerf, M.; Kraft, M.; Werner, F.; Riedel, A.; Rock, G.; Mallick, K. Revisiting Crop Water Stress Index Based on Potato Field Experiments in Northern Germany. *Agric. Water Manag.* **2022**, *269*, 107664. [CrossRef]
44. Maguire, M.S.; Neale, C.M.U.; Woldt, W.E.; Heeren, D.M. Managing Spatial Irrigation Using Remote-Sensing-Based Evapotranspiration and Soil Water Adaptive Control Model. *Agric. Water Manag.* **2022**, *272*, 107838. [CrossRef]
45. Allen, R.; Pereira, L.; Raes, D.; Smith, M. Crop Evapotranspiration Guidelines for Computing Crop Requirements. FAO Irrig. Drain. Report Modeling and Application. *J. Hydrol.* **1998**, *285*, 19–40.
46. Deutscher Wetterdienst (DWD). RADOLAN Overview. 2017. Available online: https://www.dwd.de/DE/leistungen/radolan/radolan_info/radolan_poster_201711_en_pdf.pdf;jsessionid=3E21031A63B2D2123ACBCFB4786B5CDA.live11042?__blob=publicationFile&v=2 (accessed on 11 July 2025).
47. Heinrich, I.; Balanzategui, D.; Bens, O.; Blasch, G.; Blume, T.; Böttcher, F.; Borg, E.; Brademann, B.; Brauer, A.; Conrad, C.; et al. Interdisciplinary Geo-Ecological Research across Time Scales in the Northeast German Lowland Observatory (TERENO-NE). *Vadose Zone J.* **2018**, *17*, 180116. [CrossRef]
48. Zacharias, S.; Loescher, H.W.; Bogena, H.; Kiese, R.; Schrön, M.; Attinger, S.; Blume, T.; Borchardt, D.; Borg, E.; Bumberger, J.; et al. Fifteen Years of Integrated Terrestrial Environmental Observatories (TERENO) in Germany: Functions, Services, and Lessons Learned. *Earth's Future* **2024**, *12*, e2024EF004510. [CrossRef]
49. Wenzel, J.L.; Conrad, C.; Piernicke, T.; Spengler, D.; Pöhlitz, J. Assessing the Impact of Different Irrigation Levels on Starch Potato Production. *Agronomy* **2022**, *12*, 2685. [CrossRef]
50. Michel, R.; Marks, A. *ZEPHYR: Ein Simulationsmodell Zur Bewässerungssteuerung*; Ingenieurbüro Boden u. Bodenwasser: Bad Freienwalde, Germany, 2009; Available online: http://www.bodenwasser.de and www.zephyr-zwei.de; (accessed on 12 September 2025).

51. Fasterholt. Fasterholt A/S Fasterhold Maskinfabrik Gunsprinkler Bedienungsanleitung FM4800H + 4900H. 2013. Available online: https://fasterholt.de/web/content/16599?unique=59182f0eb5300d28bc824c94e539cc6047acbc50&download=true (accessed on 11 July 2025).
52. Deutscher Wetterdienst (DWD). RADOLAN CDC. 2025. Available online: https://opendata.dwd.de/climate_environment/CDC/grids_germany/daily/radolan/ (accessed on 11 July 2025).
53. Deutscher Wetterdienst (DWD). RADOLAN Composite. 2025. Available online: https://www.dwd.de/DE/leistungen/radolan/radolan_info/radolan_radvor_op_komposit_format_pdf.pdf;jsessionid=3E21031A63B2D2123ACBCFB4786B5CDA.live11042?__blob=publicationFile&v=26 (accessed on 11 July 2025).
54. Künzel, A.; Mühlbauer, K.; Neelmeijer, J.; Spengler, D. WRaINfo: An Open Source Library for Weather Radar INformation for FURUNO Weather Radars Based on Wradlib. *J. Open Res. Softw.* **2023**, *11*, 9. [CrossRef]
55. Arable Labs. Arable Mark2 Sensor Measurements. 2021. Available online: https://www.arable.com/wp-content/uploads/2021/10/Arable-Mark-2-Measurements-21_05.pdf (accessed on 11 July 2025).
56. Arable Labs. Arable Mark2 Datasheet. 2020. Available online: https://www.arable.com/wp-content/uploads/2021/10/Arable-Mark-2-w_-Solar-Product-Specifications-20_10.pdf (accessed on 11 July 2025).
57. Pix4D. Pix4Dmapper Default Templates. 2024. Available online: https://support.pix4d.com/hc/en-us/articles/205319155 (accessed on 11 July 2025).
58. Planet Labs PBC. PlanetScope Product Specifications. December 2023. Available online: https://assets.planet.com/docs/Planet_PSScene_Imagery_Product_Spec_letter_screen.pdf (accessed on 29 August 2025).
59. Allen, R.; Pereira, L.; Raes, D.; Smith, M. *FAO Irrigation and Drainage Paper No. 56*; Food and Agriculture Organization of the United Nations: Rome, Italy, 1998; Volume 56, pp. 26–40.
60. Deutscher Wetterdienst (DWD). Tägliche Raster Der FAO Grasreferenzverdunstung. Version v1.0. 2023. Available online: https://opendata.dwd.de/climate_environment/CDC/grids_germany/daily/evaporation_fao/BESCHREIBUNG_gridsgermany_daily_evaporation_fao_de.pdf (accessed on 11 July 2025).
61. Müller, J.; Müller, G. Mitteilung: Beschreibung des zur Bestimmung der aktuellen Evapotranspiration von Kulturpflanzenbeständen erarbeiteten Modells. *Z. Meteorol.* **1988**, *38*, 332–337.
62. Müller, J.; Müller, G. Mitteilung: Überprüfung des Modells von J. und G. Müller am Beispiel Kartoffel auf lehmigen Sand. *Z. Meteorol.* **1988**, *38*, 361–365.
63. Müller, J.; Müller, G. Mitteilung: Ermittlung gebietsbezogener Verdunstungswerte durch Anwendung des Modells von J. Müller und G. Müller. *Z. Meteorol.* **1989**, *39*, 142–149.
64. Böttcher, F.; Müller, J.; Schmidt, M.F. *Das agrarmeteoroogische Bodenwasserhaushaltsmodell METVER—Arbeitspapier d. Dt. Wetterdienstes*; Offenbach am Main, Germany, 2010.
65. Guetschow, P.; Fuchs, C. The Use of Drones and Comparison with Other Remote Sensing Methods in Crop Production. In Proceedings of the IFMA24 Congress, Saskatchewan, SK, Canada, 7–12 July 2024; Academic Papers: Saskatoon, SK, Canada, 2024; Volume 1, pp. 97–111.
66. Elmokadem, T.; Savkin, A.V. Towards Fully Autonomous UAVs: A Survey. *Sensors* **2021**, *21*, 6223. [CrossRef] [PubMed]
67. Katkuri, A.V.R.; Madan, H.; Khatri, N.; Abdul-Qawy, A.S.H.; Patnaik, K.S. Autonomous UAV Navigation Using Deep Learning-Based Computer Vision Frameworks: A Systematic Literature Review. *Array* **2024**, *23*, 100361. [CrossRef]
68. Agrawal, J.; Arafat, M.Y. Transforming Farming: A Review of AI-Powered UAV Technologies in Precision Agriculture. *Drones* **2024**, *8*, 664. [CrossRef]
69. Bartels, F. From Drone to Done. In *Ergebniskonferenz der digitalen Experimentierfelder—Tagungsband*; Bundesanstalt für Landwirtschaft und Ernährung (BLE), Ed.; BLE: Bonn, Germany, 2024; p. 14. Available online: www.ble.de/SharedDocs/Downloads/DE/Projektfoerderung/Digitalisierung/EF_Konferenz_Tagungsband_2024.pdf (accessed on 11 July 2025).
70. Niu, H.; Hollenbeck, D.; Zhao, T.; Wang, D.; Chen, Y. Evapotranspiration Estimation with Small UAVs in Precision Agriculture. *Sensors* **2020**, *20*, 6457. [CrossRef]
71. Thorp, K.R.; Thompson, A.L.; Harders, S.J.; French, A.N.; Ward, R.W. High-Throughput Phenotyping of Crop Water Use Efficiency via Multispectral Drone Imagery and a Daily Soil Water Balance Model. *Remote Sens.* **2018**, *10*, 1682. [CrossRef]
72. Toscano, F.; Fiorentino, C.; Capece, N.; Erra, U.; Travascia, D.; Scopa, A.; Drosos, M.; D'Antonio, P. Unmanned Aerial Vehicle for Precision Agriculture: A Review. *IEEE Access* **2024**, *12*, 69188–69205. [CrossRef]
73. Tarrio, K.; Tang, X.; Masek, J.G.; Claverie, M.; Ju, J.; Qiu, S.; Zhu, Z.; Woodcock, C.E. Comparison of Cloud Detection Algorithms for Sentinel-2 Imagery. *Sci. Remote Sens.* **2020**, *2*, 100010. [CrossRef]
74. Roy, D.P.; Huang, H.; Houborg, R.; Martins, V.S. A Global Analysis of the Temporal Availability of PlanetScope High Spatial Resolution Multi-Spectral Imagery. *Remote Sens. Environ.* **2021**, *264*, 112586. [CrossRef]
75. Frazier, A.E.; Hemingway, B.L. A Technical Review of Planet Smallsat Data: Practical Considerations for Processing and Using PlanetScope Imagery. *Remote Sens.* **2021**, *13*, 3930. [CrossRef]

76. Latte, N.; Lejeune, P. PlanetScope Radiometric Normalization and Sentinel-2 Super-Resolution (2.5 m): A Straightforward Spectral-Spatial Fusion of Multi-Satellite Multi-Sensor Images Using Residual Convolutional Neural Networks. *Remote Sens.* **2020**, *12*, 2366. [CrossRef]
77. Leach, N.; Coops, N.C.; Obrknezev, N. Normalization method for multi-sensor high spatial and temporal resolution satellite imagery with radiometric inconsistencies. *Comput. Electron. Agric.* **2019**, *164*, 104893. [CrossRef]
78. Houborg, R.; McCabe, F.M. Daily retrieval of NDVI and LAI at 3 m resolution via the fusion of cubesat, landsat, and MODIS data. *Remote Sens.* **2018**, *10*, 890. [CrossRef]